Generation of global 1 km all-weather instantaneous and daily mean land surface temperature from MODIS data

Bing Li[1], Shunlin Liang[2], Han Ma[2], Guanpeng Dong[1], Xiaobang Liu[3], Tao He[4], Yufang Zhang[5]

[1] Key Research Institute of Yellow River Civilization and Sustainable Development & Laboratory of Climate Change Mitigation and Carbon Neutrality, Henan University, Zhengzhou 450046, China

[2] Department of Geography, University of Hong Kong, Hong Kong 999077, China

[3] The 27th Research Institute of China Electronics Technology Group Corporation, Zhengzhou 450047, China

[4] School of Remote Sensing and Information Engineering, Wuhan University, Wuhan 430079, China

[5] School of Software, Northwestern Polytechnical University, Xi'an 710072, China

Correspondence to: Shunlin Liang (shunlin@hku.hk)

Abstract: Land surface temperature (LST) serves as a crucial variable in characterizing climatological, agricultural, ecological, and hydrological processes. Thermal infrared (TIR) remote sensing provides high temporal and spatial resolution for obtaining LST information. Nevertheless, TIR-based satellite-LST products frequently exhibit missing values due to cloud interference. Prior research on estimating all-weather instantaneous LST has predominantly concentrated on regional or continental scales. This study involved generating a global all-weather instantaneous and daily mean LST product spanning from 2000 to 2020 using XGBoost. Multisource data, including Moderate-Resolution Imaging Spectroradiometer (MODIS) top-of-atmosphere (TOA) observations, surface radiation products, and reanalysis data, were employed. Validation using an independent dataset of 77 individual stations demonstrated the high accuracy of our products, yielding RMSEs of 2.787 K (instantaneous) and 2.175 K (daily). The RMSE for clear-sky conditions was 2.614 K

for the instantaneous product, slightly lower than the cloudy-sky RMSE of 2.931 K. Our instantaneous and daily mean LST products exhibit higher accuracy compared to the MODIS official LST product (RMSE=3.583 K instantaneous, 3.105 K daily) and the land component of the 5th generation of European ReAnalysis (ERA5-Land) LST product (RMSE= 4.048 K instantaneous, 2.988 K daily). Significant improvements are observed in our LST product, notably at high latitudes, compared to the official MODIS LST product. The LST dataset from 2000 to 2020 at the monthly scale, the daily mean LST on the first day of 2010 can be freely downloaded from https://doi.org/10.5281/zenodo.4292068(Li et al. 2024), and the complete product will be available at https://glass-product.bnu.edu.cn/.

1 Introduction:

Land surface temperature (LST) is the skin temperature of the Earth's surface, and one of the crucial parameters in the surface energy balance, and the hydrothermal cycle (Bastiaanssen et al. 1998; Tomlinson et al. 2011). LSTs retrieval from in situ measurements or satellites are widely used in many scientific fields (Kappas and Phan 2018), such as climate change (Auger et al. 2021; Weng 2009), urban heat island (Zhou et al. 2018), drought monitoring (Wan et al. 2010), longwave radiation estimation (Cheng and Liang 2016), evapotranspiration (Kalma et al. 2008; Yao et al. 2012), soil moisture estimation (Zhang et al. 2015), and air temperature estimation (Chen et al. 2021; Rao et al. 2019; Shen et al. 2020). High-precision measurements of LST aid in the recording of the long-term global temperature trends, thus, the International Geosphere and Biosphere Programme (IGBP) lists it as one of its priority parameters (Townshend et al. 2007). Owing to the complex and rapid variation in temporal and spatial scales, in situ measurements cannot provide regional LST or capture the spatial variation in LST. Remote sensing has become the only way to obtain LST with high spatial and temporal resolution from regional to global scales (Li et al. 2013).

Over the past few decades, substantial advancements have been made in the inversion of LST from remote sensing satellites. The retrieval of satellite LST products is predominantly accomplished using thermal infrared (TIR) remote sensing data (Li et al. 2013). These LST products typically exhibit a notable spatial resolution, exemplified by the Visible Infrared Imaging Radiometer Suite (VIIRS) boasting a resolution of 750 meters, the Advanced Very High Resolution Radiometer (AVHRR) with 0.05° (Li et al. 2023a; Ma et al. 2020a), and the Moderate-Resolution Imaging Spectroradiometer (MODIS) satellite with a resolution of 1 kilometer (Wan 2014; Wan and Li 1997). Nevertheless, due to the constrained penetration capability of thermal radiation, TIR data is exclusively applicable for observing LST under clear-sky conditions. Global average annual cloud coverage has been reported to exceed 70% (Mercury et al. 2012). The lack of data has significantly constrained the application of LST products. Consequently, all-weather LST estimation is one of the difficulties that need to be solved urgently.

Besides data gaps due to cloud contamination, extending the temporal scale of LST poses a significant challenge in retrieving LST remote sensing products, requiring urgent attention. LST, a dynamic physical attribute, exhibits temporal variation. However, satellite-derived LST captures only instantaneous observations at specific times and angles. Instead of focusing solely on instantaneous LST,

67   certain researchers emphasize the importance of daily, monthly, or yearly average LST to track the impact

68   of increasing LST on glaciers, ice sheets, and vegetation within the Earth's ecosystem (Lawrimore et al.

69   2011). Currently, for MODIS LST products, there exist daily instantaneous L2 products, daily gridded

70   instantaneous L3 products, and eight-day synthetic products (Wan 2014). Nevertheless, there's an

71   absence of L4 products encompassing daily mean, monthly, and annual LST data. Hence, it holds

72   significant importance to estimate daily mean LST based on limited MODIS observations. Acquiring the

73   daily mean LST allows estimation of monthly or annual mean LST, crucial for prolonged monitoring

74   across diverse research domains like climate change, agriculture, and drought studies.

75   As for filling LST gaps under cloudy-sky conditions, researchers have explored various methods

76   (Li et al. 2023c). One type of approach is based on space-time information, such as interpolation and

77   fusion methods (Pede and Mountrakis 2018). Interpolation methods usually utilize temporally or

78   spatially proximate clear-sky pixel information to fill in the pixels under the cloudy-sky condition.

79   Nevertheless, the efficacy of the interpolation method is contingent upon the accessibility of clear-sky

80   pixels. The reconstruction outcomes prove less satisfactory in instances of extensive missing regions or

81   prolonged periods of cloud cover (Metz et al. 2014; Zhang et al. 2018; Zhang et al. 2022). In recent years,

82   spatiotemporal fusion methods have been explored for obtaining all-weather LST(Chen et al. 2015; Long

83   et al. 2020; Wu et al. 2019). The essence of spatiotemporal fusion for LST involves deriving high spatial

84   resolution LST at time t0 from its counterpart with coarse spatial resolution at the identical time instance,

85   achieved through the application of a scale conversion factor (Long et al. 2020; Wu et al. 2019). Due to

86   the algorithm's complexity, fusion methods are commonly evaluated within limited geographical scopes,

87   with their applicability constrained when extended to larger areas. Furthermore, both interpolation and

88   spatiotemporal fusion methods hinge on information derived from clear-sky pixels, yielding

89   reconstructed theoretical clear-sky LST rather than the real cloudy-sky LST. In order to obtain actual

90   LST under cloudy-sky conditions, one type of approach considering the physical processes of the surface

91   energy balance (SEB). Jin and Dickinson (2000) introduced a method utilizing SEB to account for

92   changes in solar radiation on LST during cloudy conditions. This approach corrects clear-sky LST using

93   the SEB equation to derive actual cloudy-sky LST. Over time, the SEB-based method has been refined

94   for geostationary satellites (Jia et al. 2022; Liu et al. 2023; Zhang et al. 2024) and MODIS data (Jia et al.

95   2021; Yu et al. 2014; Zeng et al. 2018). However, widespread application is limited due to gaps in data

96   coverage and the necessity of meteorological SEB parameters (e.g., air temperature, wind speed), which

97   are challenging to obtain accurate data on a large scale.

98   Apart from the mentioned methods for LST retrieval under cloudy-sky conditions, alternative

99   approaches utilize all-weather data like microwave data, reanalysis data, or model simulations to derive

100   the cloudy-sky information. Passive microwave (PMW) data are less affected by cloud contamination,

101   providing a possibility for all-weather LST estimations (Duan et al. 2017b; Holmes et al. 2009). However,

102   the existing microwave observations usually have coarse resolutions (e.g., AMSR-E with 25km) (Mao

103   et al. 2007). Since the land surface microwave emissivity is sensitive to land surface characteristics and

104   difficult to measure, the accuracy of the PMW LST data is relatively lower than that of TIR

105   LST(McFarland et al. 1990).In addition, PMW data basically have swath gaps, especially at low latitudes,

106   which makes it difficult to obtain full-coverage LST (Holmes et al. 2009; Zhou et al. 2015). Thus, LST

107   retrieval from PMW data cannot satisfy the requirements of high-precision and refined applications.

108   Some scholars have explored the possibility of combining PMW and TIR data to estimate all-weather

109   LST. These methods perform well at regional or national scales (Duan et al. 2017b; Wu et al. 2022; Xu

110   and Cheng 2021; Zhang et al. 2020). However, owing to the availability of PMW data and the complexity

111   of algorithms, it is difficult to achieve long-term production at a global scale.

112   In comparison, reanalysis data can provide another way for all-weather LST estimation, with all-

113   weather observations, long-term and seamless characteristics. With the updating of reanalysis and

114   modeled data, spatial resolution and accuracy are improved (Muñoz-Sabater et al. 2021). Several studies

115   have attempted to utilize reanalysis data combined with TIR (Long et al. 2020; Tang et al. 2024; Zhang

116   et al. 2021) and PMW data (Zhang et al. 2020; Zhou et al. 2022) to obtain all-weather LST, which were

117   well implemented on the regional scale. In recent years, researchers have a growing interest in the

118   estimation of global all-weather LST. Shiff et al. (2021) integrated modeled temperature data to

119   supplement missing values in MODIS LST using the Google Earth Engine (GEE). Nevertheless, the

120   proposed approach solely addressed missing pixels, potentially introducing border effects. Globally,

121   continuous spatiotemporal LST data at a resolution of 0.05° have been generated, rectifying reconstructed

122   missing data under cloudy-sky conditions using reanalysis data (Yu et al. 2022). Additionally, global

123   seamless 8-day and monthly average LST data, featuring a 30 arcsecond resolution, were created by

124   integrating reanalysis data (Yao et al. 2023). These studies confirm the potential of reanalysis data for

125 estimating all-weather LST, yet there remains ample room for exploration at a spatiotemporal scale of

126 one kilometer per day.

127   Regarding daily mean LST, researchers have investigated acquiring it from polar-orbiting satellites.

128 Specifically, they have employed MODIS instantaneous LSTs to estimate the daily mean

129 LST(Williamson et al. 2014; Xing et al. 2021). The maximum-minimum method determined the daily

130 mean LST by averaging its maximum and minimum values, exhibiting a strong correlation with surface

131 air temperature (Williamson et al. 2014). Despite its relatively low accuracy, it presents a straightforward

132 means of estimating daily mean LST using the limited observations from polar orbiting satellites.

133 Another approach involves the diurnal temperature cycle (DTC), employing various nonlinear models

134 based on heat conduction and energy balance equations(Aires et al. 2004; Duan et al. 2012; Inamdar et

135 al. 2008; Sun and Pinker 2005), capable of retrieving daily mean LST. However, the DTC method

136 requires specific satellite observation counts within a daily cycle, existing challenges for all-weather

137 daily mean LST retrieval, especially for polar-orbiting satellites. Hong et al. (2021) proposed a

138 framework combining the annual temperature cycle (ATC) and DTC to retrieve all-weather daily mean

139 LST at a spatial resolution of $0.5°\times0.5°$ (Hong et al. 2022). Xing et al. (2021) utilized global in situ

140 measurements and multiple linear regression to enhance the MODIS daily mean LST model accuracy

141 under clear-sky conditions. Then, Li et al. (2023b) integrated pre-2000 polar-orbiting satellite data to

142 improve the global daily mean LST model. Most mentioned methods are applicable exclusively under

143 clear-sky conditions, and all-weather estimation remains a challenge. Besides, the sine or cosine assumed

144 in the DTC and the multiple linear regression equations may not necessarily fit the relationship between

145 instantaneous observations and daily mean value. Thus, more appropriate relational models need to be

146 constructed. The main limitation of MODIS daily mean LST estimation has been their restricted

147 observations. MODIS data in swath type can provide more observations, which potentially improving

148 the accuracy, but few researchers have attempted it. Obtaining all-weather daily mean LST from polar-

149 orbiting satellite observations (e.g., MODIS), particularly at a global scale with a 1 km spatial resolution,

150 still remains a significant challenge.

151   Recently, machine learning and deep learning techniques have gained significant traction in remote

152 sensing due to their superior model fitting capabilities (Ma et al. 2019; Yuan et al. 2020). Scholars have

153 investigated LST retrieval using learning techniques across various satellite platforms (Li et al. 2021; Ma

154   et al. 2024; Mao et al. 2018; Wang et al. 2010). However, the majority of these methods utilized clear-

155   sky pixels as the true value to construct the model, possibly failing to capture the relationship under

156   cloudy-sky conditions. Additionally, learning methods have not yet been applied for estimating daily

157   mean LST. Our former research has estimated all-weather LST from MODIS data using a random forest

158   over the conterminous United States (Li et al. 2021). Considering the urgency of obtaining all-weather

159   LST on a large regional scale and expanding the daily mean time scale, this study refined our previously

160   developed algorithm for an all-weather instantaneous LST product and developed a new method for a

161   daily mean LST product at a global scale. The improvements over our previous study include: 1) More

162   sufficient information: MODIS top-of-atmosphere (TOA) information was taken into account; 2) Expand

163   the estimated LST time scale: a novel algorithm was proposed to estimate both instantaneous and daily

164   mean LST; and 3) Higher efficiency algorithm and larger region: the global all-weather LST products

165   were generated.

166   The rest of the paper is organized as follows. Section 2 describes the data used in this paper. Section

167   3 provides a summary of the proposed method. The results are presented in Section 4. A discussion part

168   is presented in Section 5. Section 6 is the data availability. Finally, Section 7 presents the conclusions.

169

2 Data

171   In this study, the remote sensing data, reanalysis data and in situ measurements from 2002-

172   2018 were used to construct all-weather LST models. These data, spanning 2000 to 2020, along

173   with the developed models, were used to generate the instantaneous and daily mean LST products.

174   In situ measurements validated the accuracy of the proposed algorithm and the generated products.

175   The data used are described in detail as follows:

176   **2.1 Remotely sensed and reanalysis data**

177   The remote sensing data and reanalysis data used in this study are summarized in Table 1. Among

178   them, remote sensing data are mainly from official MODIS products and the Global LAnd Surface

179   Satellite (GLASS) product suite. MOD021KM and MYD021KM are MODIS TOA observational

180   datasets. The shortwave bands (B1–B7, B19) and longwave bands (B27–B36) were selected as model

181   inputs. Geolocation information was obtained from MODIS geolocation data (MOD03 and MYD03).

182   The coordinates from MODIS geolocation data were used to match up with products and in situ

183   measurements, while height, solar zenith angle, solar azimuth angle, view zenith angle and view azimuth

184   angle were used as the model inputs. MODIS LST (MOD11L2/MYD11L2) was used for the comparison

185   and identification of cloudy-sky conditions. The GLASS product suite includes at least 12 land surface

186   variables, which have high spatial resolutions (1 km and 0.05°), long-term temporal coverage (1981–

187   present), spatial continuity, and high quality (Liang et al. 2021; Liang et al. 2013a; Liang et al. 2013b).

188   In this study, we used the following four products from the GLASS product suite: Broad band emissivity

189   (BBE), broadband albedo (albedo), downward solar radiation (DSR), and downward thermal radiation

190   (LWDN). BBE product was used to obtain in-situ LST (Cheng and Liang 2013, 2014). Albedo was used

191   as the model input to describe surface characteristics (Liu et al. 2013a; Qu et al. 2016; Qu et al. 2014).

192   Because LST is affected by both solar radiation and surface longwave radiation, DSR and LWDN were

193   also used in the model construction (Cheng et al. 2017; Zhang et al. 2019).

194   In recent years, an enhanced global dataset for the land component of the fifth generation of

195   European ReAnalysis (ERA5-Land) has been developed (Hersbach et al. 2020; Muñoz-Sabater et al.

196   2021). ERA5-Land describes a consistent long terms evolution of water and energy cycles over land. It

197   was generated through global high-resolution numerical integrations of the European Centre for

198   Medium-Range Weather Forecasts (ECMWF) land surface model driven by the downscaled

199 meteorological forcing from the ERA5 climate reanalysis. Compared with the previous ERA-Interim (80

200 km) and ERA (31 km), ERA5-Land has a higher spatial resolution (9 km) and temporal resolution (1 h).

201 Because ERA5-Land LST includes worldwide and all-weather data, it was used in the model construction

202 as the background value and was also used for comparison. ERA5-Land LST is hereafter referred to as

203 ERA LST.

204

Table 1. Summary of remote sensing and reanalysis data

Product	Variables	Resolution (temporal /spatial)	Temporal coverage	Usage	Data link
MOD021KM /MYD021KM	Toa reflectance, brightness temperature	Instantaneous /1 km	2000-present for MODIS Terra / 2002-present for MODIS Aqua	Model inputs	https://earthdata.nasa.gov/
MOD03/ MYD03	Latitude, longitude, height,	Instantaneous /1 km		Model inputs/match up	
MOD11L2/ MYD11L2	LST	Instantaneous /1 km		Comparison	
GLASS	BBE	8 days/1km	2000-2022	Calculate in situ LSTs	http://glass.umd.edu/ or https://glass-product.bnu.edu.cn/
GLASS	Albedo	8 days/1km	2000-2022	Model inputs	
GLASS	DSR	Daily/0.05°	2000-2022	Model inputs	
GLASS	LWDN	Instantaneous /1 km	2000-2020	Model inputs	
ERA5-land	LST	1 hour/ 9 km	1981-present	Model inputs	https://cds.climate.copernicus.eu/

205

2.2 In situ measurements

207 To obtain in situ LSTs, we collected upwelling and downwelling longwave radiation measurements

208 from 315 sites with different land cover types and geolocations on a global scale. Both instantaneous and

209 daily mean in situ LSTs were retrieved from in situ measurements. As shown in Fig.1, ground

210 measurements from 238 stations were used to develop the proposed network (blue circles), whereas the

211 measurements from the remaining 77 stations (red circles) were selected as independent validation

212 datasets to evaluate the performance of the trained model. The collection sites were mainly from eight

213 observation networks, which are described in the following paragraphs.
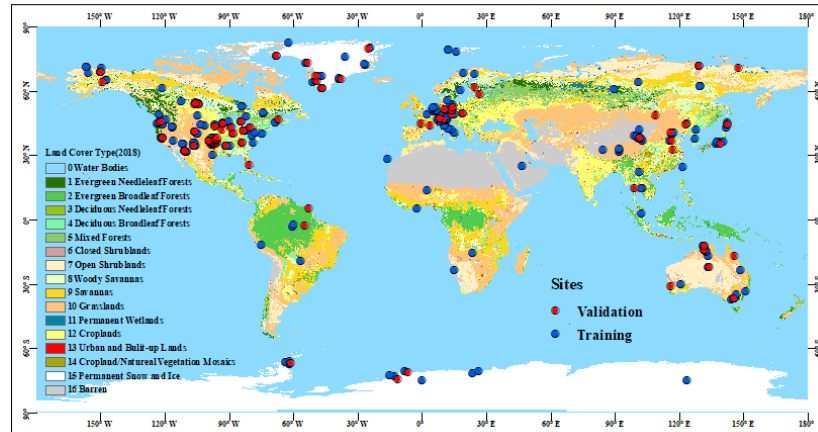
Fig.1 Spatial distribution of the selected sites at a global scale. Land use cover types of 2018 (background color shading) were from the MODIS land use cover product MCD12C1. The sites used for model training are shown with blue circles while the separated validation sites are shown with red circles.

AmeriFlux (https://ameriflux.lbl.gov/) is a network of stations that continuously measures ecosystem carbon dioxide, water, energy fluxes, and related environmental variables using eddy covariance techniques (Baldocchi 2003). The network was launched in 1996 and was established to connect research on field sites representing major climate and ecological biomes(Boden et al. 2013). The network has more than past and present flux towers, and sites with longwave radiation measurements were selected. These sites are distributed across North, Central, and South America. The observation interval of these sites was half an hour.

FLUXNET (https://fluxnet.org/) is a global network of micrometeorological tower sites that uses eddy covariance methods to measure carbon dioxide, water vapor, and energy fluxes (Baldocchi et al. 2001). It has more than 500 flux towers worldwide are operating on a long-term basis. The overarching goal of the FLUXNET data collection is to provide information for validating remote sensing products, such as net primary productivity and energy fluxes. Sites with longwave radiation records were used in this study. The observation interval of the sites was half an hour.

The Baseline Surface Radiation Network (BSRN, https://bsrn.awi.de/) is a project of the Data and Assessments Panel of the Global Energy and Water Cycle Experiment (GEWEX) under the umbrella of the World Climate Research Programme (WCRP) (Ohmura et al. 1998). The purpose of this network is to provide validation materials for satellite radiometry and climate models. It further aims to detect long-term variations in the radiation field at the Earth's surface, which play a vital role in climate changes (Driemel et al. 2018). The stations (currently 74 in total, 58 active) are distributed in contrasting climatic

237 zones, covering a latitude range from 80° N to 90° S. The required longwave radiation measurements

238 were obtained with high accuracy and high time resolution (1 – 3 minutes).

239 AsiaFlux (https://www.asiaflux.net/) is a scientific community with the aim of developing

240 collaborative research and datasets on carbon, water, and energy cycles in key Asian ecosystems.

241 AsiaFlux has grew from a small network in 1999 to a multi-national science community with more than

242 400 members from 28 countries (Yamamoto 2005). Currently, there are 109 flux towers in Asia, and

243 more sites are underway. The biomes covered in AsiaFlux range from rainforests near the equator to

244 tundra in the Arctic and Antarctic, and from wetlands near sea level to grasslands at high altitudes, such

245 as the Tibetan Plateau. Most sites have a time resolution of 0.5 hour, while 15 minutes and 1 hour are

246 used for individual sites.

247 The Atmospheric Radiation Measurement (ARM, https://www.arm.gov/) Program, supported by the

248 U.S. Department of Energy, is a project for atmospheric measurement and modeling. The purpose of the

249 project was to detect processes that affect atmospheric radiation and describe these processes in climate

250 models (Stokes and Schwartz 1994). The quantities measured at these stations included longwave and

251 shortwave radiation, clouds properties, water vapor, other radiation-related quantities, and

252 meteorological variables. These sites had the high temporal resolution of 1 minute.

253 The Ice and Climate group at the Institute for Marine and Atmospheric Research of Utrecht

254 University (UU/IMAU, https://www.projects.science.uu.nl/iceclimate/) has deployed several Automatic

255 Weather Stations (AWS) on different glaciers around the world (Antarctica, Greenland, Alps, Norway,

256 Iceland, Svalbard), and in different climate regimes. The stations were designed to operate on a long-

257 term basis and measure meteorological and radiation variables in remote regions under harsh weather

258 conditions. The main purpose of these stations is to detect the energy balance in these regions in view of

259 climate change and, sea-level variation. The stations from the IMAU project have time resolutions of 1

260 and 2 hours.

261 Denmark launched the Programme for Monitoring of the Greenland Ice Sheet (PROMICE,

262 https://www.promice.dk/) to detect variations in the mass balance of the Greenland ice sheet. Several

263 weather stations were established on the ice sheet to provide filed data for modeling and validation. The

264 weather stations were equipped with CNR1 or CNR4 instruments to measure radiation data with a time

265 resolution of 10 minutes.

266   The National Tibetan Plateau Data Center (TPDC, http://data.tpdc.ac.cn) has integrated and released

267   various scientific data from the Qinghai-Tibet Plateau and surrounding regions. Integrated data resources

268   include the atmosphere, cryosphere, hydrosphere, and energy balance. Among these data sources, there

269   are various published ground measurements. We selected several stations in the Heihe Basin (Liu et al.

270   2018), Haihe Basin (Liu et al. 2013b), and Qinghai-Tibet Plateau (Ma et al. 2020b). The time resolutions

271   of these stations were 10 minutes, 30 minutes and 1 hour, respectively.

272   Some stations from various flux networks overlapped, and we curated observations with extended

273   time series and heightened time resolution. Attaining high model accuracy necessitates superior in situ

274   measurements, necessitating rigorous quality assessment. Initially, adjacent stations potentially causing

275   interference were removed, alongside the manual elimination of anomalous observations and

276   discontinuous measurements. Subsequently, the collection sites were strategically dispersed globally.

277   Fig.2 depicts a histogram illustrating the distribution of land cover types and climate zones across the

278   sites. Each land cover type was accounted for, and additional sites encompassing water bodies were

279   incorporated to estimate LST for inland water. The stations were dispersed across five distinct climate

280   zones, with a higher concentration in temperate and continental climates. Importantly, we meticulously

281   gathered data from numerous high-latitude stations within a polar climate to address substantial

282   estimation uncertainties in the area.
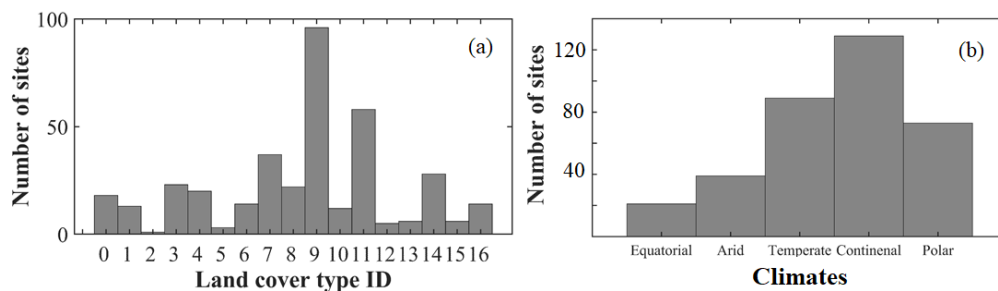
283

284   Fig.2 Land cover types (a) and climate zones (b) of sites (The land surface type represented by the x-axis in (a) refers to the
285   legend in Fig.1

286

287

3 Methods

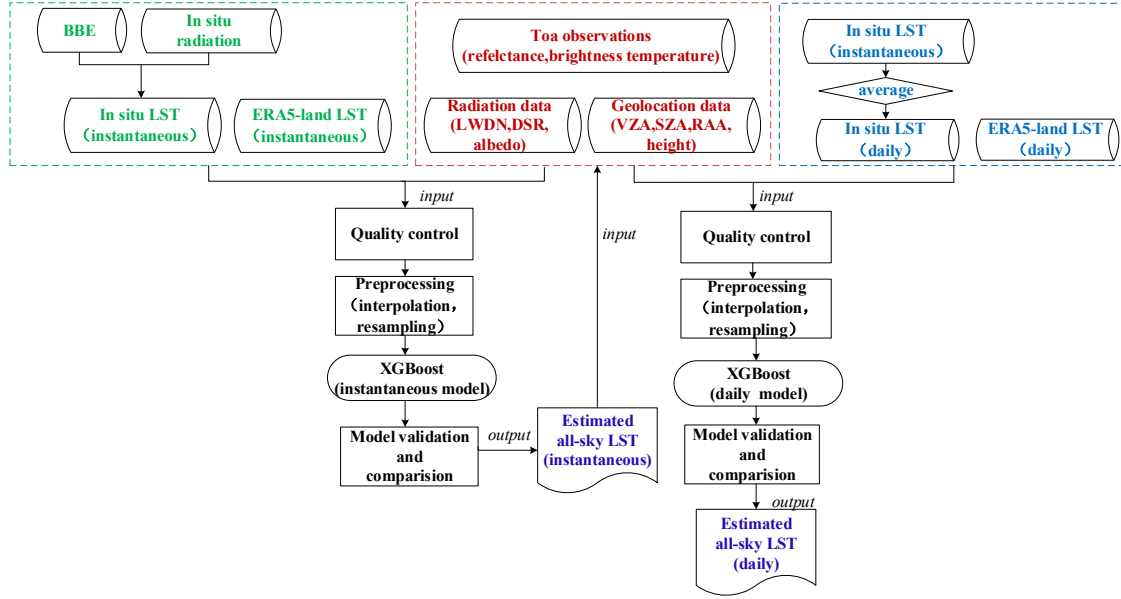The study's comprehensive framework is depicted in Fig.3. Initially, the in situ LST and remote sensing data underwent preprocessing and pairing. Subsequently, the data pairs were randomly divided into two segments: one for model training and validation, while the other served as an independent dataset for model evaluation. The XGBoost algorithm was employed to sequentially develop models for instantaneous and daily mean LST, while also conducting parameter tuning. The estimated all-weather instantaneous LST served as an input for the daily mean LST model. Ultimately, the optimal models underwent separate evaluation and comparison with alternative products.

Fig.3 Flowchart of the XGBoost algorithm for all-weather instantaneous and daily mean LST estimation.

3.1 Data Preprocessing

3.1.1 In situ instantaneous LST

The in situ LST in this study was calculated from surface broadband emissivity and in situ upwelling and downwelling longwave radiation, according to Stefan–Boltzmann's law, as follows:

$$T_S = \left(\frac{F_{up} - (1-\varepsilon)F_{dn}}{\sigma\varepsilon}\right)^{\frac{1}{4}} , \qquad (1)$$

where T_S represents the in situ LST, F_{up} is the upwelling longwave radiation, and F_{dn} is the downwelling longwave radiation, ε is surface broadband emissivity, and σ is the Stefan-Boltzmann constant (5.67×10^{-8} W/m²/K⁴).

Surface broadband emissivity was acquired from the GLASS BBE product through nearest

interpolation to derive daily values. F_{up} and F_{dn} were derived from in situ measurements. Due to varying observation intervals across different networks, spanning from 1 minute to 1 hour, a linear interpolation method was applied to determine the in situ LST corresponding to the MODIS satellite observation time.

3.1.2 Daily mean LST

To construct a daily mean LST model, in situ daily mean LST and ERA daily mean LST are required. Once the instantaneous LST from in situ measurements was obtained, the daily mean in situ LST was calculated according to Eq. (2). The ERA daily mean LST was obtained using Eq. (3).

$$LST_{DS} = \frac{1}{n}\sum_{i=1}^{n} LST(i)_{IS} \tag{2}$$

$$LST_{DE} = \frac{1}{24}\sum_{i=1}^{24} LST(i)_{IE} \tag{3}$$

LST_{DS} and LST_{DE} represent the daily mean in situ LST and ERA daily mean LST respectively, and n is the count of the in situ measurements per day. LST_{IS} and $LST(i)_{IE}$ are the instantaneous in situ LST values calculated from Eq. (1) and ERA LST, respectively. If the in situ measurements were incomplete in a day, the record for that day was not used.

One traditional daily mean LST method, which was retrieved from the official MODIS Aqua LST for both daytime and nighttime (Williamson et al. 2014), was used for comparison. The equation can be expressed as follows:

$$LST_{DM} = 0.5 * LST_{AD} + 0.5 * LST_{AN} \ , \tag{4}$$

where LST_{DM} represents the retrieval of the daily mean LST, and LST_{AD} and LST_{AN} represent the daytime and nighttime LST, respectively from the official MODIS Aqua LST.

3.1.3 Data normalization

Due to discrepancies in spatial and temporal resolutions among the utilized products, preprocessing was conducted. Albedo and BBE had an 8-day temporal resolution, and the daily data were acquired through nearest interpolation. DSR and ERA LST were adjusted to a spatial resolution of 1 km via the nearest-neighbor method. The ERA LST, with a temporal resolution of 1 hour, was interpolated linearly to obtain the reanalysis LST at the satellite observation time. Matching of in situ measurements and satellite data was performed based on coordinates from MOD03/MYD03 products.

3.2 Developing the estimation algorithm

Extreme Gradient Boosting (XGBoost) is an effective and scalable gradient boosting implementation introduced by Chen and Guestrin (2016). It amalgamates multiple classification and regression trees to create a robust learner. In regression, the initial tree is constructed based on split features, followed by the creation of subsequent trees to capture residuals from the preceding ones. Additional trees are iteratively generated until they meet the stopping criteria. Notably, the regression trees within XGBoost are interrelated, progressively diminishing the residuals of predictions with new trees. The ultimate prediction is derived by aggregating scores from each tree.

In contrast to the random forest method, which also employs decision trees (Breiman 2001), XGBoost operates in parallel. Its algorithm design incorporates column blocks for parallel learning, cache-aware access, and facilitates out-of-core computation, substantially boosting computational efficiency. Owing to XGBoost's notable efficiency and precision, many studies in remote sensing have adopted this algorithm for regression tasks (Kim et al. 2021; Liu et al. 2021; Zhang et al. 2023). In this research, XGBoost was implemented using the Scikit-learn package in Python. Experiments were performed on a computer equipped with a 3.60 GHz CPU and 64 GB RAM, utilizing the same dataset and features. Detailed hyperparameters are elucidated in Section 3.3.

3.3 Model development

The dataset for 2002-2018 were compiled at a global scale. Samples from 238 sites were randomly chosen for model training. The remaining samples from 77 sites were used as independent dataset for the model validation. The features used to construct the instantaneous LST model, included MODIS TOA observations, ERA LST, DSR, LWDN, albedo, and geolocation data. MODIS TOA observations were used to describe the contributions of shortwave and longwave radiation to the LST, which is greatly changed with solar radiation influenced by clouds. Hence, DSR was used to reflect the effect of solar radiation on the LST (Zeng et al. 2018). Longwave radiation is less affected by the atmosphere, has a certain penetration, and has a close correlation and interaction with the LST during the daytime and nighttime. In this study, the LWDN was used to reflect the effect of thermal infrared radiation on LST. LST is also influenced by land cover types, and broadband albedo was used to represent land surface characteristics. In addition, geolocation information, such as solar angles, view angles and height, also

362   affects LST retrieval from satellites. All the input variables were all-weather conditions with high

363   resolution. In addition, ERA LST can provide all-weather LST, but with coarse resolution (0.1°). It was

364   considered as a background field and, provided an initial value for the model. After the instantaneous

365   model was constructed, the daily mean model was developed. Research has confirmed linear or nonlinear

366   relationships between the daily mean LST and instantaneous LSTs for polar orbiting satellites (Duan et

367   al. 2014; Xing et al. 2021). Hence, the instantaneous retrieval of all-weather LST data was used in the

368   daily LST model. In addition, the ERA daily LST rather than the ERA LST was used as the initial value

369   in the daily LST model. Except for these two variables, the inputs of the two models were the same.

370   Specifically, the daily mean LST was finally retrieved from the average of multiple observations in one

371   day.

372   Model tuning was performed to prevent over-fitting of the models. Several hyper-parameters in

373   XGBoost needed to be tuned, including the number of gradient boosted trees (n_estimators), maximum

374   depth of trees (Max_depth), the minimum sum of weights of all observations required in a child

375   (Min_child_weight), minimum loss reduction required to make a split (gamma), the fraction of

376   observations to be random samples for each tree (subsample), the fraction of columns to be randomly

377   sampled for each tree (Colsample_bytree). Lambda and alpha represent the regularization of the weights

378   in XGBoost, which can improve the speed performance. A random search combined grid search was used

379   to tune the model. Table 2 presents the candidate values of the random search and the final settings for

380   the two LST models.

381   Table 2. Candidate values and selected values of hyper-parameters in XGBoost

Hpyer-parameter	Candidate values	Selected values	
	(start, end, step)	Instantaneous model	Daily model
n_estimators	50,401,10	160	140
Max_depth	1,10,1	9	9
Min_child_weight	1,10,1	5	6
gamma	0,1,0.1	0.8	0.5
subsample	0.1,1,0.1	1	1
Colsample_bytree	0.1,1,0.1	0.8	0.8
lambda	0.1, 2, 0.1	0.6	1.4
alpha	0.1, 2, 0.1	1.6	1.19

382

383   **3.4 Evaluation approaches**

384   In this study, validation from training and independent datasets of separated ground measurements

385   was used to evaluate the instantaneous and daily mean LST models. A widely used ten-fold cross

386   validation (10-CV) method was used to evaluate the stability of the models. Then, model performance

387   was assessed for different weather conditions, and observation times. In addition, time series of

388   individual sites and spatial distribution at regional and global scales were chosen to further demonstrate

389   the effectiveness of the developed models. Finally, the proposed framework and generated products were

390   compared with those of previous studies and products.

4 Results

4.1 Model training and validation

In general, 70% of the dataset was used for the model training. The remaining dataset was used for

model adjustment and validation. Independent validation and 10-CV results were used to evaluate the

models. Fig.4 and Fig.5 show the accuracies of the instantaneous and daily mean LST models,

respectively. From the scatter density plots, all the validation results for both the instantaneous and daily

models are close to the 1:1 line, with R^2 values ranging from 0.974 to 0.990. The Root Mean Squared

Error (RMSE) of the training and validation results were 2.413 K and 2.787 K for the instantaneous

model, while 1.758 K and 2.175 K for the daily mean LST model. Both models showed high accuracy

in model training and validation, with no obvious overfitting. The 10-CV method is also used to

comprehensively validate the models and the results of both models are also satisfactory, with RMSEs

=2.421 K and 1.808 K for the instantaneous and daily mean LST models, respectively. Overall, the

validations from the independent dataset and 10-CV results show acceptable accuracy and robustness of

the two models. Both models are robust. The daily mean LST model shows a higher accuracy than the

instantaneous LST model. Probably because the daily mean LST is obtained by averaging multiple

observations in one day, which reduces the uncertainty. In addition, some daily inputs (daily mean in situ

LST and ERA LST) used in the daily model have less uncertainty than instantaneous observations.
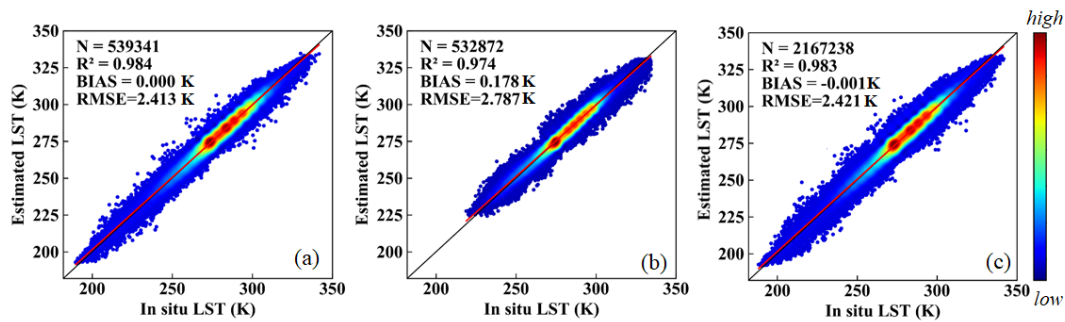
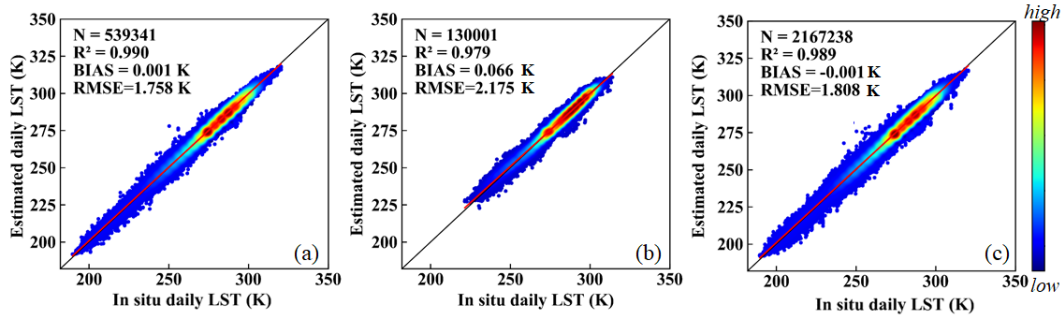Fig.4 The (a) training, (b) independent validation and (c) 10-CV results of the instantaneous LST model

Fig.5 The (a) training, (b) independent validation and (c) 10-CV results of the daily mean LST model

In addition, we further verify the model performance under different conditions using an independent dataset. Table 3 presents the validation results for different observation times and satellites for the instantaneous model. The RMSEs are 3.03 K and 2.67 K for daytime and nighttime data respectively. The accuracy of nighttime data is higher than that of daytime data. It probably because of the absence of differential solar heating and higher spatial-temporal heterogeneity in daytime (Duan et al. 2019; Liu et al. 2023). In addition, the LST value during the daytime is higher than that during nighttime, which results in a higher RMSE value. For the validation of the MOD and MYD satellites, the RMSE of the MOD is nearest to that of the MYD. We further verify the accuracy in the presence and absence of clouds; the density plots are shown in Fig.6. The accuracy under clear-sky conditions was relatively higher with an RMSE= 2.614 K, whereas the RMSE is 2.931 K under cloudy-sky conditions. More effective observation information and higher accuracy of inputs under clear-sky conditions, result in a higher accuracy of clear-sky estimation. This phenomenon is also present in other studies (Duan et al. 2023; Ma et al. 2024). Furthermore, to explore whether clouds have an effect on daily mean LST retrieval, we calculate the accuracy under different cloud proportions, as shown in Table 3. The results show that the RMSE values increased slightly as the proportion of cloudy-sky observations increased. This demonstrates that cloud contamination has a limited impact on the daily mean LST estimation in the proposed method.

Table 3. Validation for different observation times, satellites and weather conditions of instantaneous the model, and the proportion of cloudy-sky MODIS observations of the daily mean LST model

	Groups	R^2	RMSE (K)	Bias (K)
	Daytime	0.960	2.99	0.30
Instantaneous LST model	Nighttime	0.980	2.61	0.05
	MOD	0.980	2.80	0.19

19

	MYD	0.980	2.82	0.17
Daily mean LST model	0-30	0.980	2.01	-0.07
(Proportion of cloudy	30-60	0.980	2.14	-0.16
MODIS observations %)	60-100	0.980	2.26	-0.04
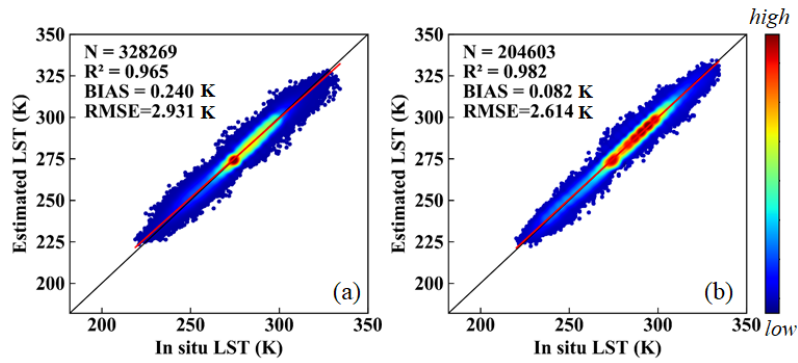
Fig.6 Validation under (a) cloudy-sky conditions and (b) clear-sky conditions

4.2 Validation and assessment
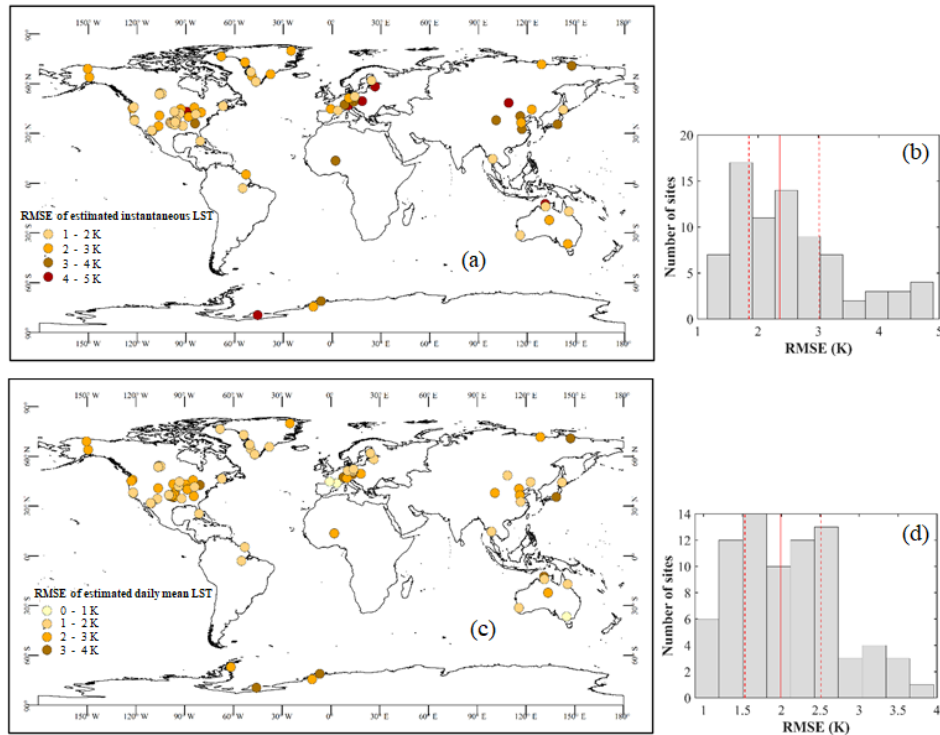
4.2.1 Evaluation across individual sites

The validation of the instantaneous and daily mean LST for individual sites is shown in Fig.7. The color of the circles indicates the increasing level of errors. RMSEs rank from 1.16 to 4.90 K for instantaneous LST and 0.89 to 3.96 K for daily mean LST. The corresponding histograms show that the accuracy of nearly 75% of sites is below 3 K and 2.5 K for instantaneous and daily mean LST, respectively. Stations distributed in the continental United States with intensive LST monitoring generally have higher accuracy. High accuracy is also observed at stations in Alaska and Greenland, whereas a relatively lower accuracy is observed in the Antarctic. In Europe, most stations perform well, with the exception of some stations in the east. The stations in Asia are relatively discrete with relatively lower accuracy for individual sites in western China, which is probably due to the high elevation and complex terrain (Jia et al. 2023). In addition, several stations distributed in Australia, Africa, and South America also perform well in both models. In general, the results indicate a satisfactory predictive ability of both instantaneous and daily mean LST models at most individual sites.

Fig.7 Validation of individual sites for instantaneous LST (a), daily mean LST (c) and their corresponding histograms (b, d)

4.2.2 Evaluation across land cover types and elevation

LST is closely related to land cover types. The validation results for different land cover types are presented in Table 4. The results indicated that the data had high accuracies for most land cover types. For instantaneous LST, the RMSEs of most vegetation types were below 3 K, except for shrublands with an RMSE of 3.04 K. Among the vegetation types, cropland had an outstanding RMSE of 2.55 K. The accuracies of vegetation types for daily mean LST were higher than that of instantaneous LST, with RMSEs of approximately 2 K, except for shrublands with an RMSE of 2.55 K. The accuracy in water bodies was also satisfactory, with RMSEs of 2.43 and 2.04 K for instantaneous and daily mean LST, respectively. For both models, the accuracy of instantaneous and daily mean LST in snow/ice with RMSE of 2.94 and 2.35 K, respectively were notably improved compared with that found in our previous study (Li et al. 2021). This is probably due to the higher number of samples from high latitudes, which improved the model robustness in snow/ice. However, the accuracy for urban and barren areas was relatively low. This is likely due to the high heterogeneity of urban areas, high albedo and low specific heat capacity of barren land (Duan et al. 2017a). In general, for different land cover types, the daily mean model showed higher accuracy than the instantaneous model, and both models had acceptable accuracy. In addition, we summarized the accuracy of the different elevation ranges in Table 5. The results indicate

21

that elevation has an impact on LST retrieval accuracy. The relatively poor accuracy at high elevations

is probably due to the harsh natural environment and complex terrain, which was also reflected in another

study (Zhao et al. 2019).

Table 4. Validation of instantaneous and daily mean LST models for various land cover types

	Instantaneous LST model			Daily mean LST model		
	R^2	RMSE (K)	Bias (K)	R^2	RMSE (K)	Bias (K)
Forest	0.941	2.82	0.11	0.960	2.08	-0.11
Shrublands	0.980	3.04	-1.05	0.980	2.55	-0.85
Savannas	0.960	2.74	0.12	0.980	2.13	0.24
Grassland	0.960	2.65	0.12	0.960	2.02	0.06
Wetland	0.980	2.87	-0.86	0.980	2.19	-0.35
Cropland	0.960	2.55	-0.05	0.960	2.22	0.06
Urban	0.774	3.76	0.4	0.883	2.51	-0.44
Snow	0.941	2.94	0.77	0.960	2.35	0.69
Barren	0.941	3.8	0.95	0.960	3.53	0.85
Water	0.960	2.43	-0.34	0.980	2.04	-0.22

Table 5. Validation of the instantaneous and daily mean LST models for different elevations

	Instantaneous LST			Daily mean LST		
Elevation (m)	R^2	RMSE (K)	Bias (K)	R^2	RMSE (K)	Bias (K)
<500	0.960	2.63	-0.06	0.980	2.14	0.12
500-1000	0.980	2.85	0.60	0.980	2.16	-0.35
1000-2000	0.980	3.25	0.39	0.980	2.29	-0.41
>2000	0.941	3.79	-0.83	0.941	2.74	1.23

4.2.3 Comparison with other products

Official MODIS and ERA LST data were used for comparison with our LST products. Fig.8 presents

the accuracy of ERA LST (RMSE = 4.048 K) and official MODIS LST (RMSE = 3.583 K), both of

which were lower than the accuracy of the estimated LST proposed in this study (RMSE = 2.787 K,Fig.4).

Furthermore, we noted that the official MODIS LST data had several abnormal points (Fig.8.(b)). The

polar regions (Antarctica and the Arctic pole) were verified separately from the other regions, as shown

in Fig.9. The results indicate that the majority of outliers were from stations located in Antarctica and the

Arctic pole (Fig.9.(b)), probably because of cloud contamination. Owing to the spectral similarities

between the ice and snow, the misjudgment of clouds leads to cloud top temperatures rather than LST

(Liu et al. 2010; Østby et al. 2014). In contrast, the proposed method was unaffected by cloud

contamination (Fig.9 (a)).
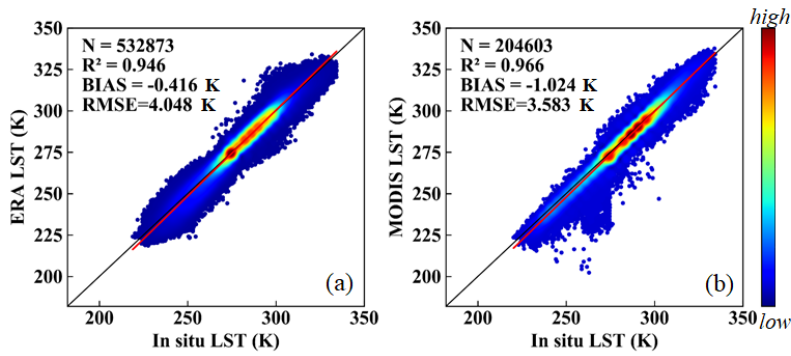
487

488   Fig.8 Density plots of (a) ERA LST and (b) MODIS clear-sky LST

489
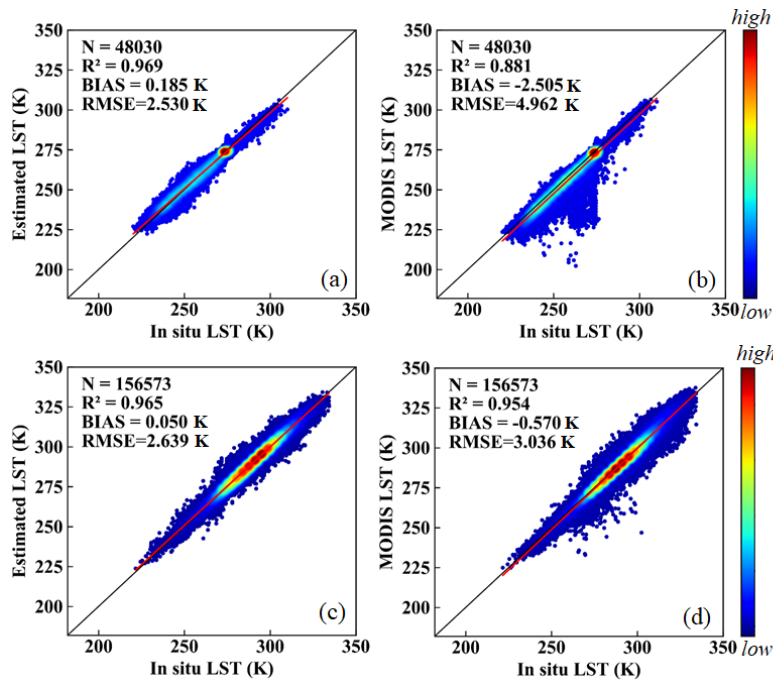
490   Fig.9 Density plots of estimated instantaneous clear-sky LST (a, c) and MODIS LST (b, d) in polar regions (first row) and

491   other regions (second row)

492   The daily mean LST from the ERA LST from Eq. (3), and official MODIS LST from Eq. (4)) were

493   used for comparison (Fig.10). The ERA daily LST had an acceptable accuracy, with an RMSE of 2.988

494   K. The RMSE of the daily mean official MODIS LST was 3.105 K. The accuracy of the MODIS official

495   LST was relatively lower compared to what was reported in a previous study. This may be due to the

496   large uncertainty in the official MODIS LST in polar regions. When removing the observations in polar

497   regions, the accuracy improved with an RMSE of 2.799 K, similar to the result in previous studies

498   (Williamson et al. 2014; Xing et al. 2021). The proposed method in this study has a higher accuracy than

499   the daily mean LST from ERA and official MODIS LST, with an RMSE of 2.175 K at the global scale

500   (Fig.4.(b)). Moreover, the daily mean LST obtained from official MODIS LST is only suitable under

501   clear-sky conditions, whereas the daily mean LST obtained in this study was for all-weather conditions.
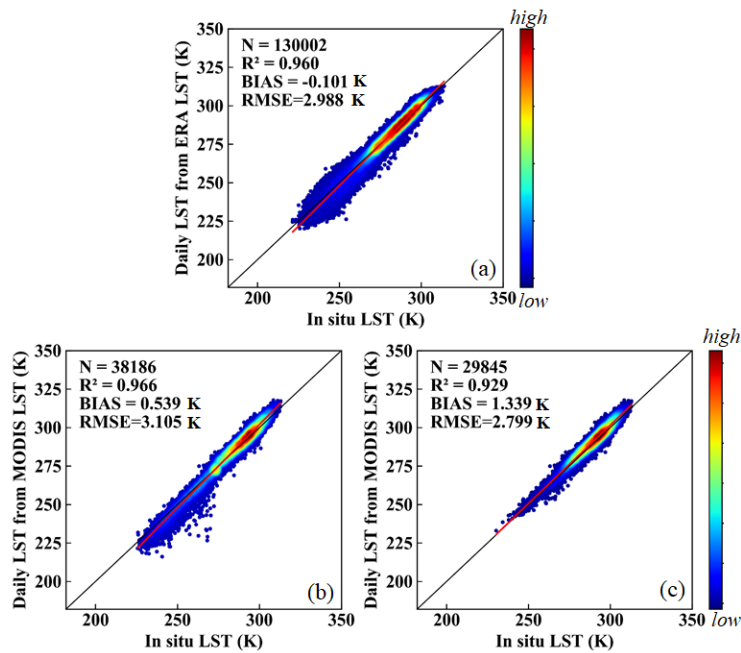
Fig.10 Density plots of (a) ERA daily mean LST and (b) official MODIS daily mean LST (c) official MODIS daily mean LST except polar regions

4.3 Spatiotemporal performance

To further evaluate the temporal performance of the estimated LST, four in situ LST measurements from different latitudes in 2010 were evaluated. Initially, instantaneous LST was examined separately for daytime and nighttime, and MODIS LST was provided for comparison (Fig.11). The RMSE values of the comparable accuracy with MODIS LST. The nighttime LST was more concentrated than the daytime LST. The estimated LST curves are in good agreement with the in situ LST and MODIS LST curves, but are more continuous than the curve of MODIS LST. Discontinuities observed at high-latitudes stations (latitude:79.835, longitude: -25.166) were due to polar day and night phenomena. The daily mean LST was also examined using in situ LST measurements (Fig.12). The daily mean LST retrieved from MODIS official LST were used for comparison. The results indicated higher accuracy and better consistency compared to instantaneous LST. The estimated daily LST also depicted more complete curves than the daily mean LST from MODIS LST, and captured the seasonal variation trends. The results demonstrate that both the estimated instantaneous LST and daily mean LST can correctly reflect the temporal variations in LST.
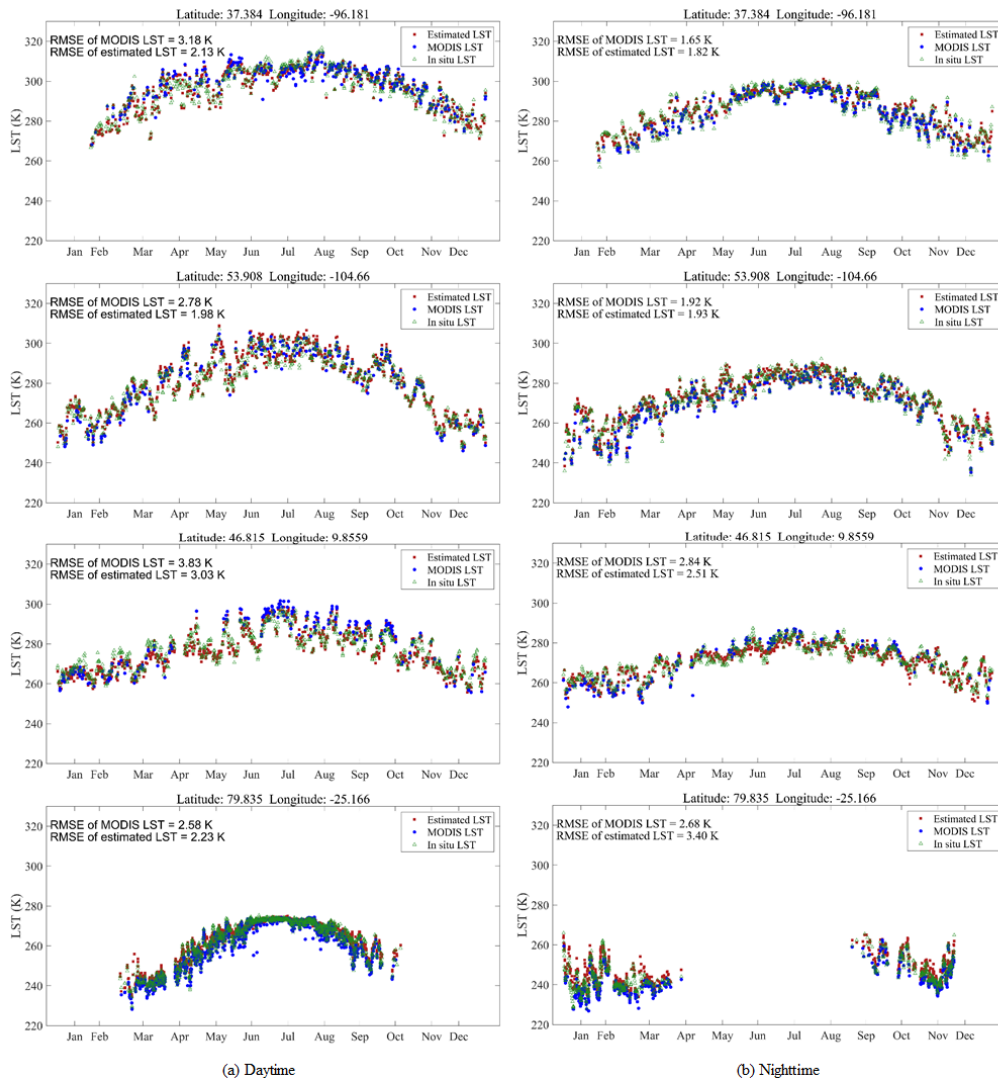
Fig.11 Time series of the estimated instantaneous LST, MODIS LST, and in situ LST at four sites from different regions in 2010: (a) daytime, (b) nighttime.
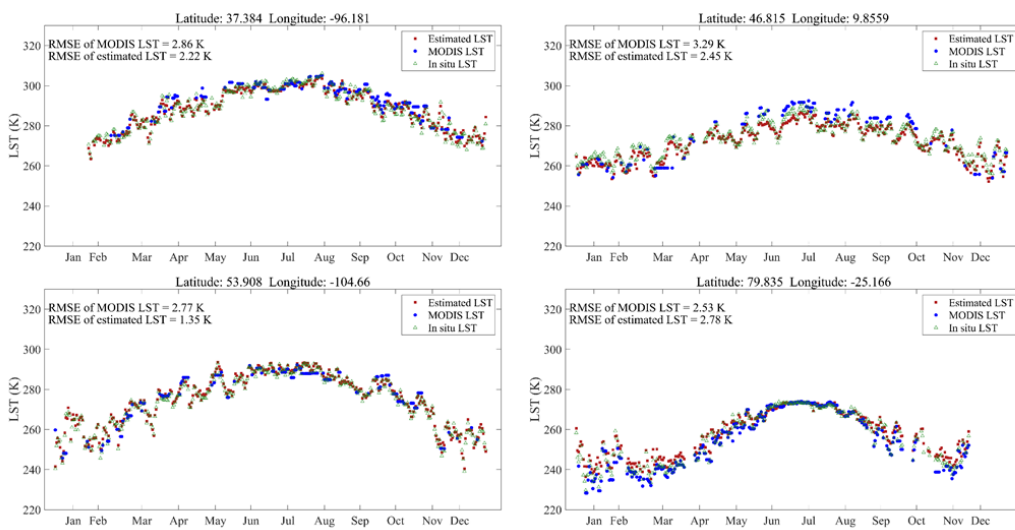

Fig.12 Time series of the estimated daily mean LST, daily mean LST retrieved from MODIS LST, and in situ LST at four sites from different regions in 2010

To further evaluate the spatial performance of the proposed methods, regional distributions and

25

526   global maps were compared. Fig.13 and Fig.14 present the spatial details of the estimated instantaneous

527   LST and daily mean LST from tiles H10V04, H23V04 and H24V05. One of the grids, H24v05, is located

528   on the Tibetan Plateau and contains mountainous terrain. The instantaneous and daily mean LST from

529   ERA LST and MODIS LST were used for comparison. MODIS LST had missing values caused by cloud

530   contaminants for both instantaneous and daily mean LST, while our method achieved spatially

531   continuous estimation. In addition, the estimated LSTs had spatial patterns similar to those of MODIS

532   LST under clear-sky conditions. Compared with the ERA LST, which was used as the model input, our

533   results showed more spatial details and corrected the underestimation in some regions. In particular, the

534   results of H24v05 reflect that the estimated LST has mountainous details. Demonstrates that our approach

535   applies to mountainous regions with high heterogeneity. The spatial details of the daily mean LST show

536   similar conclusions (Fig.14). However, there may exist boundary effects in some complex terrains, which

537   is probably due to the introduction of ERA data with coarse resolution. Overall, for both instantaneous

538   and daily mean LST, the proposed methods executed the spatially contiguous LST and, depicted the

539   spatial LST details and variations.
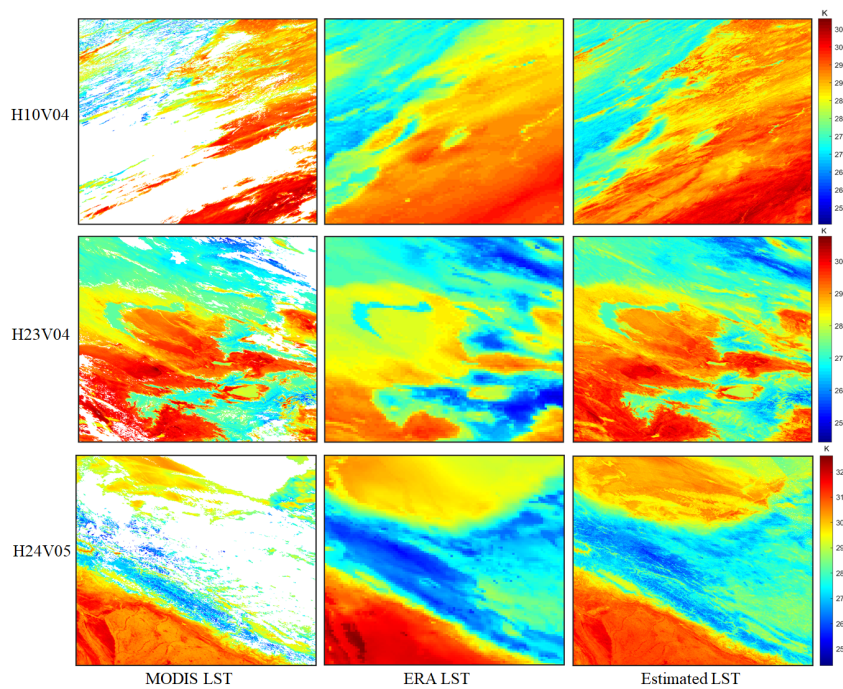
540

541   Fig.13 Spatial details of the MODIS LST, ERA LST and estimated instantaneous LST of three tiles, H10V04 (the first row),

542   H23V04 (the second row) and H24V05 (the third row) from the ninetieth day in 2010

543

MODIS daily mean LST   ERA daily mean LST   Estimated daily mean LST
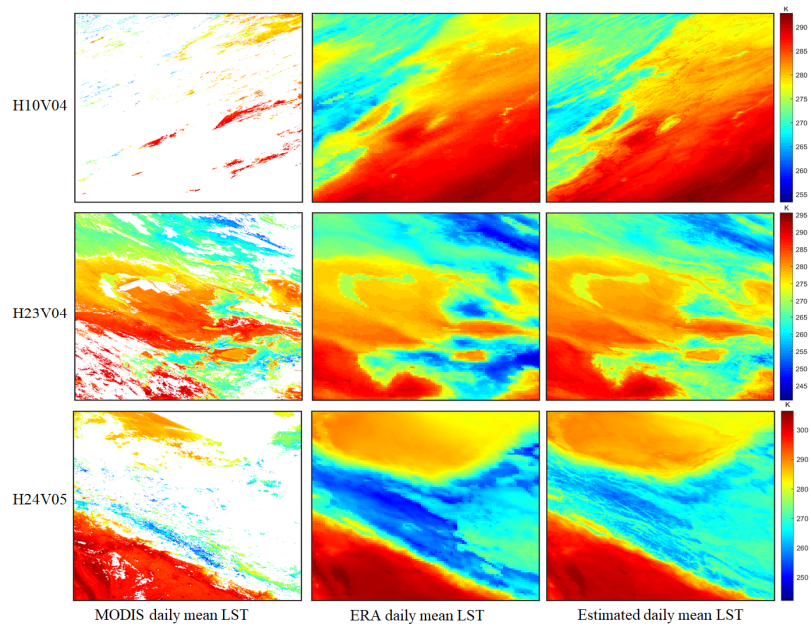
Fig.14 Spatial details of the daily mean LST retrieved from MODIS LST, ERA LST and estimated daily mean LST of three tiles H10V04 (first row), H23V04 (the second row) and H24V05 (the third row) from the ninetieth day in 2010.

Urban heat island effect is one of the main applications of LST data. To further assess the spatial details of the estimated all-weather LST and the potential of urban heat island applications, we selected four cities in different regions around the globe. And demonstrated the estimated LST in conjunction with the boundary of urban regions extracted by using global artificial impervious area data (Li et al. 2020), as shown in Fig.15. The figure shows that the built-up areas of four cities present higher LST than the periphery, and confirms that our estimated all-weather LST can capture the urban heat island phenomenon and present relevant details.
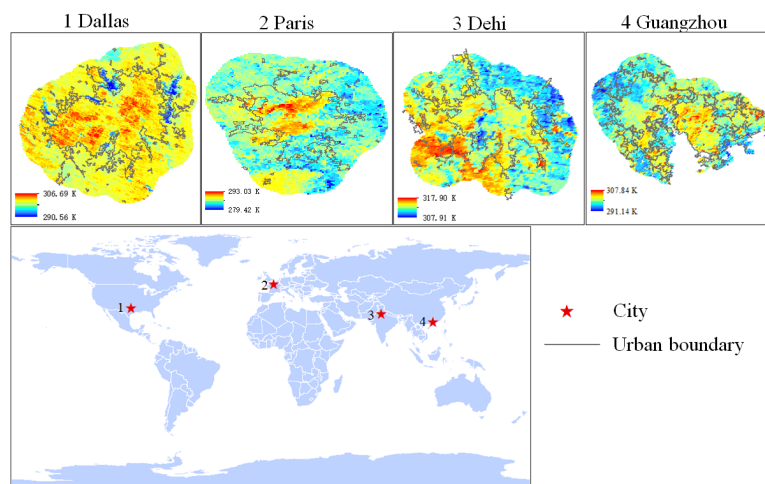

Fig.15 Spatial pattern of the estimated all-weather LST in four representative cities. The black lines are the boundary of urban regions extracted by using global artificial impervious area data.

In addition, Fig.16 and Fig.17 show the estimated instantaneous and daily mean LST at the global

27

scale on Days 90 and 270 of 2010. The instantaneous and daily mean LST from MODIS LST are shown

for comparison. The estimated instantaneous and daily LST had similar spatial patterns to the

corresponding LST from MODIS. All of the results reflected broad spatiotemporal variations. For

instance, LSTs were relatively higher at middle and low latitudes, and lower in the Arctic and Antarctic.

The instantaneous LST exhibited a larger range than the daily mean LST. In addition, the proposed

method achieved the all-weather LST retrievals. For instantaneous LST (Fig.16), a small number of gaps

in tropical regions were due to the polar-orbiting satellite configuration. The daily mean LST (Fig.17)

was spatially continuous. Overall, the proposed instantaneous LST and daily mean LST perform well on
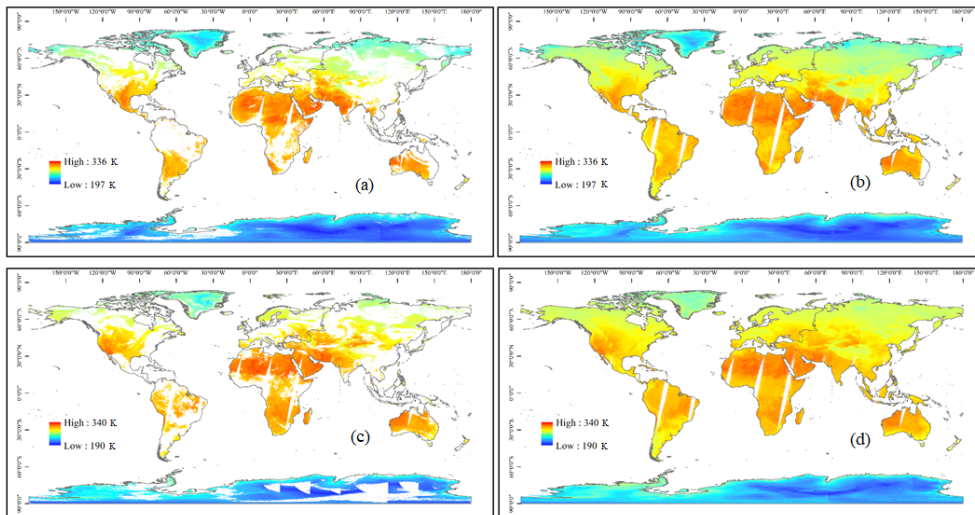
a global scale.

Fig.16 Spatial patterns of MODIS LST (a, c) and estimated instantaneous LST (b, d) at a global scale on the Days 90 (first row) and 270 (second row) of 2010.
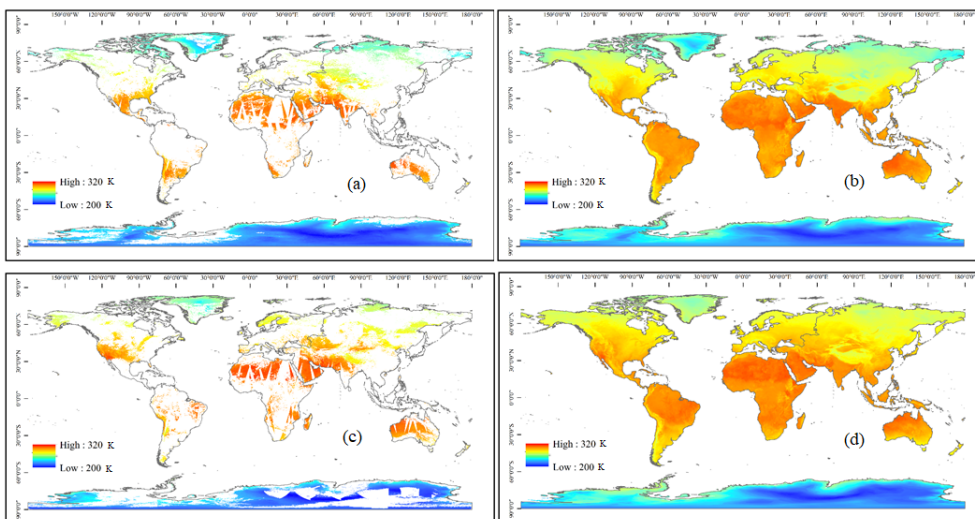
Fig.17 Spatial patterns of daily mean LST retrieved from (a, c) MODIS LST and (b, d) estimated daily mean LST at a global scale on Days 90 (first row) and 270 (second row) of 2010.

28

5 Discussion

573

574   Although several LST satellite products have been published, they are missing data under cloudy-

575   sky conditions. Existing research on all-weather LST has mostly been conducted at the regional scale.

576   This study proposes a highly accurate and efficient algorithm to retrieve all-weather LST at a global scale

577   from multi-source data, including MODIS TOA, surface radiation, reanalysis and in situ data. An all-

578   weather daily mean LST algorithm was also proposed. Both the estimated instantaneous and daily mean

579   LST had acceptable accuracy. In addition, it performs well based on independent ground measurements

580   and space-time verification.

581   **5.1 Effect of introducing MODIS TOA information and ERA LST**

582   In view of the complexity of global climate conditions, and to include more information to estimate

583   the all-weather LST, we introduced MODIS TOA data on the basis of using surface variables. In addition,

584   since the Global Land Data Assimilation System (GLDAS) LST used in previous studies did not have

585   global coverage (the Antarctica region was missing), we introduced the ERA LST in this study, which

586   not only has global coverage, but also has a higher spatio-temporal resolution (0.1°,1 h). We conducted

587   experiments with combinations of different features, to clarify the effect of introducing MODIS TOA

588   information and ERA LST under different weather conditions. A comparison of the removal of ERA LST

589   and MODIS TOA data in the models is shown in Table 6. The results show that when the ERA LST and

590   TOA data were removed, the accuracy of the model was greatly reduced. The RMSEs increased from

591   2.787 to 3.536 K and 3.466 K when ERA LST and TOA data were removed, respectively. However, the

592   accuracy changes in the two feature combinations under different weather conditions were significantly

593   different. When ERA LST was eliminated, although the accuracies of both weather conditions were

594   reduced, the RMSE increase for the cloudy sky (0.95 K) was significantly greater than that for the clear

595   sky (0.09 K). When the TOA data was removed, the results were the opposite. The accuracy of clear-sky

596   LST estimation decreased significantly. Overall, introducing MODIS TOA information and ERA LST

597   significantly improved the model accuracy. In addition, it can be inferred that ERA LST provides more

598   effective information for cloudy-sky LST estimation, while TOA data contributes more to clear-sky

599   conditions.

600

601

Table 6. The accuracy of the independent dataset with different feature combinations for the instantaneous LST model

Feature combination	All-weather			Clear sky			Cloudy sky		
	RMSE (K)	Bias (K)	R^2	RMSE (K)	Bias (K)	R^2	RMSE (K)	Bias (K)	R^2
All features	2.787	0.178	0.974	2.614	0.082	0.982	2.931	0.240	0.965
No ERA LST	3.536	-0.012	0.959	2.730	-0.14	0.980	3.950	0.07	0.941
No Toa data	3.466	0.335	0.960	3.620	0.21	0.960	3.360	0.41	0.960

5.2 Effect of station density on the model accuracy

To further evaluate the station density on the model accuracy, experiments were conducted with different station densities. Firstly, the stations were reduced randomly in the training dataset, and the model performance was evaluated based on the same test samples. The accuracies of the instantaneous and daily mean models are shown in the Table 7. The result shows that the accuracy of both models decreases as the number of stations in the training sample decreases. When the number of stations in the training sample is reduced from 238 to 158, the RMSE of the instantaneous model increases from 2.787 K to 2.988 K, and the RMSE of the daily model increases from 2.374 K to 2.479 K. The experiment indicates the model accuracy is affected by the station density, but to a limited extent when there is a sufficient amount of samples. It may be that the long time series of station data used in the experiment provided relatively sufficient samples.

Table 7.The training and testing accuracy of instantaneous and daily mean LST with the number of stations decreasing in the model training.

| training stations	training samples	instantaneous model			daily mean model		
		RMSE (K)	Bias (K)	R^2	RMSE (K)	Bias (K)	R^2
238	1797803	2.787	0.178	0.974	2.374	0.100	0.978
218	1609953	2.828	0.203	0.974	2.397	0.121	0.978
198	1420496	2.867	0.211	0.973	2.421	0.116	0.977
178	1327160	2.877	0.243	0.973	2.426	0.140	0.977
158	1072730	2.988	0.239	0.971	2.479	0.160	0.976

5.3 Effect of multiple MODIS observations

In contrast to most studies using MODIS data in sinusoidal projection, we used swath-type MODIS data to estimate daily mean LST in this study. MODIS swath data can provide more observations, particularly at high latitudes. Furthermore, we statistically analyzed the relationship between the daily mean LST model error and MODIS observation frequency. Fig.18 shows that the error decreased with

621 an increase in the MODIS observation frequency. For high-latitude areas with more observations, the

622 model accuracy at high latitudes was improved. This demonstrates the superiority of using MODIS data

623 in swath types with more observations to construct a daily mean LST model.
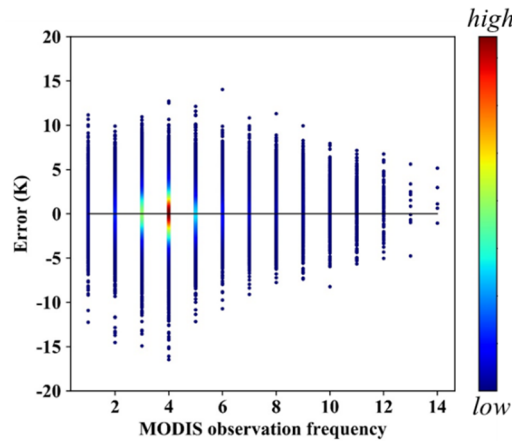
624

625 Fig.18 Density plots of daily mean LST model error with respect to MODIS observation frequency

626 **5.4 Effect of in situ measurements in the model**

627 In contrast to previous studies that used machine learning algorithms, in situ measurements were

628 used to construct the model instead of clear-sky MODIS LST. In situ measurements can obtain the real

629 LST under cloudy-sky conditions, without obtaining the hypothetical LST from clear-sky MODIS LST.

630 In addition, LST from in situ measurements is close to hemispherical LST, or observing the LST from

631 the zenith. In contrast, MODIS LST is a directional LST with view angles ranging from $0°$ ups to $>60°$,

632 resulting in a significant thermal radiation directionality (TRD) effect (Cao et al. 2019; Ermida et al.

633 2017). This results in a difference in the LST of the same object at different observation angles.

634 Theoretically, the proposed instantaneous LST weakens the influence of the TRD effect, which was been

635 confirmed in our previous study (Li et al. 2021).

636 **5.5 Effect of the new algorithm on product generation**

637 In previous study, the random forest algorithm (RF) was used to estimate the all-weather LST over

638 the conterminous United States (Li et al. 2021). Although the RF algorithm performs well, the application

639 efficiency needs to be considered for generating global products. Hence, the model accuracy and

640 efficiency were compared using RF and XGBoost. The model accuracies of RF and XGBoost was

641 comparable, with RMSEs of 2.787 K and 2.801 K, respectively (Table 8). However, training the

642 XGBoost model significantly less time, taking up 3.33 minutes compared to 60.01 minutes for RF

training. XGBoost also had an outstanding performance in the model application. As an example, to produce 100 LST swath-type images, the XGBoost took 8.93 minutes while the RF model took 38.85 minutes (Table 8). Considering the quantities of swath files at the global scale, XGBoost is a better choice for long-sequence product generation, with high accuracy and efficiency.

Table 8 Comparison of algorithms of model accuracy and efficiency.

Algorithm	Model accuracy			Model efficiency	
	RMSE (K)	Bias (K)	R^2	Training time(minute)	Application time (minute)
XGBoost	2.787	0.178	0.974	3.33	8.93
RF	2.801	0.196	0.974	60.01	38.85

5.6 Limitations

However, this study has certain limitations. Despite enhancements in LST accuracy on ice and snow surfaces, accuracy remains comparatively lower in barren and urban areas. Additionally, while the study aimed to select the highest possible number of representative ground stations for the long-term sequence, the spatial distribution was non-uniform, potentially impacting the generality of data-driven models. Furthermore, the accuracy of the high-altitude model was marginally lower, possibly attributed to the complex climatic environment and topographic conditions. For mountainous areas with complex terrain, there may be boundary effects, which is probably due to the reanalysis data with coarse resolution. Future investigations could employ advanced methods, such as deep learning, to develop a more adaptive model incorporating spatial and temporal information. Moreover, integration with other satellite sensors has the potential to extend the temporal-spatial resolution and time span of all-weather LST products.

6 Data availability

660

661   The global all-weather LST data at monthly scale from 2000-2020 can be freely downloaded from

662   https://doi.org/10.5281/zenodo.4292068(Li et al. 2024), the daily mean LST on the first day of year 2010

663   is freely available at (Li et al. 2024), all the data will be available at https://glass-

664   product.bnu.edu.cn/dload.html.

665

7 Conclusion

666

667 LST is a crucial parameter of the Earth's energy budget, and current LST satellite products are

668 affected by cloud contamination, resulting in missing values. This study attempted to retrieve all-weather

669 instantaneous and daily mean LST at a global scale. A new framework that generating global, long-

670 sequence LST product is proposed. Multiple all-weather datasets from MODIS TOA observations,

671 surface radiation data, geolocation data, reanalysis data, and ground measurements were used to construct

672 the models.

673 Based on the XGBoost algorithm and multisource data from 2002-2018, all-weather instantaneous

674 and daily mean LST models were successively built. The validation of the independent dataset showed

675 high accuracy. The ten-fold cross validation demonstrated the robustness of the models. For the

676 instantaneous LST model, clear-sky LST showed higher accuracy than cloudy-sky LST, while cloud

677 contamination had limited effects on daily mean LST estimations. Both models performed well for most

678 land cover types and geolocation conditions. The time series for validation at the four sites from different

679 regions was temporally contiguous. The results showed high consistency with in situ measurements and

680 the corresponding official MODIS LST. The spatial distributions of MODIS tiles showed more spatial

681 details than the ERA LST. Global mapping illustrated spatial continuity and similar patterns with

682 instantaneous and daily mean LST from the official MODIS LST data.

683 Compared with previous products, adding TOA observations effectively improved the accuracy of

684 the instantaneous model, especially under clear-sky conditions. Moreover, multiple effective swath-type

685 observations from the MODIS data significantly improved the accuracy of the daily mean LST model.

686 In contrast to the MODIS and ERA LST, the proposed all-weather method has a higher accuracy and is

687 less affected by cloud contamination, especially at high latitudes. In terms of product generation,

688 XGBoost has higher precision and efficiency compared with RF, and provides effective support for mass

689 data production.

690 Overall, the proposed models were effective and robust, demonstrating the potential of estimating

691 all-weather instantaneous and daily mean LST from multisource data. The constructed models can be

692 used to generate long-sequence LST products from 2000 to present. The generated product is a 1 km all-

693 weather instantaneous and daily mean LST products at a global scale. It has great significance for studies

694 on climate change, surface energy balance, and many other scientific fields. In the future, new methods

695   involving spatial and temporal information, as well as other satellite sensors, should be considered to

696   expand the spatiotemporal monitoring capabilities of LST products.

697

698 **Competing Interest**

699   Author Han Ma is a member of the editorial board of the journal.

700

Reference

Aires, F., Prigent, C., & Rossow, W.B. (2004). Temporal interpolation of global surface skin temperature diurnal cycle over land under clear and cloudy conditions. *Journal of Geophysical Research: Atmospheres, 109*, 313-331

Auger, M., Morrow, R., Kestenare, E., Sallee, J.B., & Cowley, R. (2021). Southern Ocean in-situ temperature trends over 25 years emerge from interannual variability. *Nat Commun, 12*, 514

Baldocchi, D., Falge, E., Gu, L., Olson, R., Hollinger, D., Running, S., Anthoni, P., Bernhofer, C., Davis, K., Evans, R., Fuentes, J., Goldstein, A., Katul, G., Law, B., Lee, X., Malhi, Y., Meyers, T., Munger, W., Oechel, W., Paw, K.T., Pilegaard, K., Schmid, H.P., Valentini, R., Verma, S., Vesala, T., Wilson, K., & Wofsy, S. (2001). FLUXNET: A New Tool to Study the Temporal and Spatial Variability of Ecosystem–Scale Carbon Dioxide, Water Vapor, and Energy Flux Densities. *Bulletin of the American Meteorological Society, 82*, 2415-2434

Baldocchi, D.D. (2003). Assessing the eddy covariance technique for evaluating carbon dioxide exchange rates of ecosystems: past, present and future. *Glob Chang Biol, 9*, 479-492

Bastiaanssen, W.G., Menenti, M., Feddes, R., & Holtslag, A. (1998). A remote sensing surface energy balance algorithm for land (SEBAL). 1. Formulation. *Journal of Hydrology, 212*, 198-212

Boden, T.A., Krassovski, M., & Yang, B. (2013). The AmeriFlux data activity and data system: an evolving collection of data management techniques, tools, products and services. *Geoscientific Instrumentation, Methods and Data Systems, 2*, 165-176

Breiman, L. (2001). Random forests. *Machine Learning, 45*, 5-32

Cao, B., Liu, Q., Du, Y., Roujean, J.-L., Gastellu-Etchegorry, J.-P., Trigo, I.F., Zhan, W., Yu, Y., Cheng, J., Jacob, F., Lagouarde, J.-P., Bian, Z., Li, H., Hu, T., & Xiao, Q. (2019). A review of earth surface thermal radiation directionality observing and modeling: Historical development, current status and perspectives. *Remote Sensing of Environment, 232*

Chen, B., Huang, B., & Xu, B. (2015). Comparison of Spatiotemporal Fusion Models: A Review. *Remote Sensing, 7*, 1798-1835

Chen, T., & Guestrin, C. (2016). Xgboost: A scalable tree boosting system. In, *Proceedings of the 22nd acm sigkdd international conference on knowledge discovery and data mining* (pp. 785-794)

Chen, Y., Liang, S., Ma, H., Li, B., He, T., & Wang, Q. (2021). An all-sky 1 km daily surface air temperature product over mainland China for 2003–2019 from MODIS and ancillary data. *Earth System Science Data*

Cheng, J., & Liang, S. (2013). Estimating global land surface broadband thermal-infrared emissivity using advanced very high resolution radiometer optical data. *International Journal of Digital Earth, 6*, 34-49

Cheng, J., & Liang, S. (2014). Estimating the broadband longwave emissivity of global bare soil from the MODIS shortwave albedo product. *Journal of Geophysical Research: Atmospheres, 119*, 614-634

Cheng, J., & Liang, S. (2016). Global Estimates for High-Spatial-Resolution

Clear-Sky Land Surface Upwelling Longwave Radiation From MODIS Data. *IEEE Transactions on Geoscience and Remote Sensing, 54*, 4115-4129

Cheng, J., Liang, S., Wang, W., & Guo, Y. (2017). An efficient hybrid method for estimating clear-sky surface downward longwave radiation from MODIS data. *Journal of Geophysical Research: Atmospheres, 122*, 2616-2630

Driemel, A., Augustine, J., Behrens, K., Colle, S., Cox, C., Cuevas-Agulló, E., Denn, F.M., Duprat, T., Fukuda, M., Grobe, H., Haeffelin, M., Hodges, G., Hyett, N., Ijima, O., Kallis, A., Knap, W., Kustov, V., Long, C.N., Longenecker, D., Lupi, A., Maturilli, M., Mimouni, M., Ntsangwane, L., Ogihara, H., Olano, X., Olefs, M., Omori, M., Passamani, L., Pereira, E.B., Schmithüsen, H., Schumacher, S., Sieger, R., Tamlyn, J., Vogt, R., Vuilleumier, L., Xia, X., Ohmura, A., & König-Langlo, G. (2018). Baseline Surface Radiation Network (BSRN): structure and data description (1992–2017). *Earth System Science Data, 10*, 1491-1501

Duan, S.-B., Li, Z.-L., Cheng, J., & Leng, P. (2017a). Cross-satellite comparison of operational land surface temperature products derived from MODIS and ASTER data over bare soil surfaces. *Isprs Journal of Photogrammetry and Remote Sensing, 126*, 1-10

Duan, S.-B., Li, Z.-L., & Leng, P. (2017b). A framework for the retrieval of all-weather land surface temperature at a high spatial resolution from polar-orbiting thermal infrared and passive microwave data. *Remote Sensing of Environment, 195*, 107-117

Duan, S.-B., Li, Z.-L., Tang, B.-H., Wu, H., Tang, R., Bi, Y., & Zhou, G. (2014). Estimation of Diurnal Cycle of Land Surface Temperature at High Temporal and Spatial Resolution from Clear-Sky MODIS Data. *Remote Sensing, 6*, 3247-3262

Duan, S.-B., Li, Z.-L., Wang, N., Wu, H., & Tang, B.-H. (2012). Evaluation of six land-surface diurnal temperature cycle models using clear-sky in situ and satellite data. *Remote Sensing of Environment, 124*, 15-25

Duan, S.-B., Lian, Y., Zhao, E., Chen, H., Han, W., & Wu, Z. (2023). A Novel Approach to All-Weather LST Estimation Using XGBoost Model and Multisource Data. *IEEE Transactions on Geoscience and Remote Sensing, 61*, 1-14

Duan, S.B., Li, Z.L., Li, H., Gottsche, F.M., Wu, H., Zhao, W., Leng, P., Zhang, X., & Coll, C. (2019). Validation of Collection 6 MODIS land surface temperature product using in situ measurements. *Remote Sensing of Environment, 225*, 16-29

Ermida, S.L., DaCamara, C.C., Trigo, I.F., Pires, A.C., Ghent, D., & Remedios, J. (2017). Modelling directional effects on remotely sensed land surface temperature. *Remote Sensing of Environment, 190*, 56-69

Hersbach, H., Bell, B., Berrisford, P., Hirahara, S., Horányi, A., Muñoz-Sabater, J., Nicolas, J., Peubey, C., Radu, R., Schepers, D., Simmons, A., Soci, C., Abdalla, S., Abellan, X., Balsamo, G., Bechtold, P., Biavati, G., Bidlot, J., Bonavita, M., Chiara, G., Dahlgren, P., Dee, D., Diamantakis, M., Dragani, R., Flemming, J., Forbes, R., Fuentes, M., Geer, A., Haimberger, L., Healy, S., Hogan, R.J., Hólm, E., Janisková, M., Keeley, S., Laloyaux, P., Lopez, P., Lupu, C., Radnoti, G., Rosnay, P., Rozum, I., Vamborg, F., Villaume, S., & Thépaut, J.N. (2020). The ERA5 global reanalysis. *Quarterly Journal of the Royal Meteorological Society, 146*, 1999-2049

Holmes, T.R.H., De Jeu, R.A.M., Owe, M., & Dolman, A.J. (2009). Land surface temperature from Ka band (37 GHz) passive microwave observations. *Journal of Geophysical Research, 114*

Hong, F., Zhan, W., Göttsche, F.-M., Lai, J., Liu, Z., Hu, L., Fu, P., Huang, F., Li, J., Li, H., & Wu, H. (2021). A simple yet robust framework to estimate accurate daily mean land surface temperature from thermal observations of tandem polar orbiters. *Remote Sensing of Environment, 264*, 112612

Hong, F., Zhan, W., Göttsche, F.-M., Liu, Z., Dong, P., Fu, H., Huang, F., & Zhang, X. (2022). A global dataset of spatiotemporally seamless daily mean land surface temperatures: generation, validation, and analysis. *Earth System Science Data, 14*, 3091-3113

Inamdar, A.K., French, A., Hook, S., Vaughan, G., & Luckett, W. (2008). Land surface temperature retrieval at high spatial and temporal resolutions over the southwestern United States. *Journal of Geophysical Research, 113*

Jia, A., Liang, S., & Wang, D. (2022). Generating a 2-km, all-sky, hourly land surface temperature product from Advanced Baseline Imager data. *Remote Sensing of Environment, 278*, 113105

Jia, A., Liang, S., Wang, D., Ma, L., Wang, Z., & Xu, S. (2023). Global hourly, 5 km, all-sky land surface temperature data from 2011 to 2021 based on integrating geostationary and polar-orbiting satellite data. *Earth System Science Data, 15*, 869-895

Jia, A., Ma, H., Liang, S., & Wang, D. (2021). Cloudy-sky land surface temperature from VIIRS and MODIS satellite data using a surface energy balance-based method. *Remote Sensing of Environment, 263*, 112566

Kalma, J.D., McVicar, T.R., & McCabe, M.F. (2008). Estimating land surface evaporation: A review of methods using remotely sensed surface temperature data. *Surveys in Geophysics, 29*, 421-469

Kappas, M., & Phan, T.N. (2018). Application of MODIS land surface temperature data: a systematic literature review and analysis. *Journal of Applied Remote Sensing, 12*, 1

Kim, M., Brunner, D., & Kuhlmann, G. (2021). Importance of satellite observations for high-resolution mapping of near-surface NO2 by machine learning. *Remote Sensing of Environment, 264*, 112573

Lawrimore, J.H., Menne, M.J., Gleason, B.E., Williams, C.N., Wuertz, D.B., Vose, R.S., & Rennie, J. (2011). An overview of the Global Historical Climatology Network monthly mean temperature data set, version 3. *Journal of Geophysical Research, 116*

Li, B., Liang, S., Liu, X., Ma, H., Chen, Y., Liang, T., & He, T. (2021). Estimation of all-sky 1 km land surface temperature over the conterminous United States. *Remote Sensing of Environment, 266*, 112707

Li, B., Liang, S., Ma, H., Liu, X., He, T., & Zhang, Y. (2024). All-weather 1km land surface temperature at global scale from 2000-2020 from MODIS data.Zenodo [Data set]. Zenodo. https://doi.org/10.5281/zenodo.4292068

Li, J.-H., Li, Z.-L., Liu, X., & Duan, S.-B. (2023a). A global historical twice-daily (daytime and nighttime) land surface temperature dataset produced by Advanced Very High Resolution Radiometer observations from 1981 to 2021. *Earth System Science*

Data, 15, 2189-2212

Li, J.-H., Li, Z.-L., Liu, X., Duan, S.-B., Si, M., Shang, G., & Zhang, X. (2023b). A generalized method for retrieving global daily mean land surface temperature from polar-orbiting thermal infrared sensor instantaneous observations. *International Journal of Remote Sensing*, 1-22

Li, X., Gong, P., Zhou, Y., Wang, J., Bai, Y., Chen, B., Hu, T., Xiao, Y., Xu, B., Yang, J., Liu, X., Cai, W., Huang, H., Wu, T., Wang, X., Lin, P., Li, X., Chen, J., He, C., Li, X., Yu, L., Clinton, N., & Zhu, Z. (2020). Mapping global urban boundaries from the global artificial impervious area (GAIA) data. *Environmental Research Letters, 15*

Li, Z.-L., Tang, B.-H., Wu, H., Ren, H., Yan, G., Wan, Z., Trigo, I.F., & Sobrino, J.A. (2013). Satellite-derived land surface temperature: Current status and perspectives. *Remote Sensing of Environment, 131*, 14-37

Li, Z.L., Wu, H., Duan, S.B., Zhao, W., Ren, H., Liu, X., Leng, P., Tang, R., Ye, X., Zhu, J., Sun, Y., Si, M., Liu, M., Li, J., Zhang, X., Shang, G., Tang, B.H., Yan, G., & Zhou, C. (2023c). Satellite Remote Sensing of Global Land Surface Temperature: Definition, Methods, Products, and Applications. *Reviews of Geophysics, 61*

Liang, S., Cheng, J., Jia, K., Jiang, B., Liu, Q., Xiao, Z., Yao, Y., Yuan, W., Zhang, X., Zhao, X., & Zhou, J. (2021). The Global Land Surface Satellite (GLASS) Product Suite. *Bulletin of the American Meteorological Society, 102*, E323-E337

Liang, S., Zhang, X., Xiao, Z., Cheng, J., Liu, Q., & Zhao, X. (2013a). *Global LAnd Surface Satellite (GLASS) products: algorithms, validation and analysis*. Springer Science & Business Media

Liang, S., Zhao, X., Liu, S., Yuan, W., Cheng, X., Xiao, Z., Zhang, X., Liu, Q., Cheng, J., Tang, H., Qu, Y., Bo, Y., Qu, Y., Ren, H., Yu, K., & Townshend, J. (2013b). A long-term Global LAnd Surface Satellite (GLASS) data-set for environmental studies. *International Journal of Digital Earth, 6*, 5-33

Liu, Q., Wang, L., Qu, Y., Liu, N., Liu, S., Tang, H., & Liang, S. (2013a). Preliminary evaluation of the long-term GLASS albedo product. *International Journal of Digital Earth, 6*, 69-95

Liu, S., Li, X., Xu, Z., Che, T., Xiao, Q., Ma, M., Liu, Q., Jin, R., Guo, J., Wang, L., Wang, W., Qi, Y., Li, H., Xu, T., Ran, Y., Hu, X., Shi, S., Zhu, Z., Tan, J., Zhang, Y., & Ren, Z. (2018). The Heihe Integrated Observatory Network: A Basin-Scale Land Surface Processes Observatory in China. *Vadose Zone Journal, 17*, 180072

Liu, S.M., Xu, Z.W., Zhu, Z.L., Jia, Z.Z., & Zhu, M.J. (2013b). Measurements of evapotranspiration from eddy-covariance systems and large aperture scintillometers in the Hai River Basin, China. *Journal of Hydrology, 487*, 24-38

Liu, W., Cheng, J., & Wang, Q. (2023). Estimating Hourly All-Weather Land Surface Temperature From FY-4A/AGRI Imagery Using the Surface Energy Balance Theory. *IEEE Transactions on Geoscience and Remote Sensing, 61*, 1-18

Liu, X., Liang, S., Li, B., Ma, H., & He, T. (2021). Mapping 30 m Fractional Forest Cover over China's Three-North Region from Landsat-8 Data Using Ensemble Machine Learning Methods. *Remote Sensing, 13*, 2592

Liu, Y., Ackerman, S.A., Maddux, B.C., Key, J.R., & Frey, R.A. (2010). Errors in Cloud Detection over the Arctic Using a Satellite Imager and Implications for

Observing Feedback Mechanisms. *Journal of Climate, 23*, 1894-1907

Long, D., Yan, L., Bai, L., Zhang, C., Li, X., Lei, H., Yang, H., Tian, F., Zeng, C., Meng, X., & Shi, C. (2020). Generation of MODIS-like land surface temperatures under all-weather conditions based on a data fusion approach. *Remote Sensing of Environment, 246*

Ma, J., Shen, H., Jiang, M., Lin, L., Meng, C., Zeng, C., Li, H., & Wu, P. (2024). A mechanism-guided machine learning method for mapping gapless land surface temperature. *Remote Sensing of Environment, 303*

Ma, J., Zhou, J., Göttsche, F.-M., Liang, S., Wang, S., & Li, M. (2020a). A global long-term (1981–2000) land surface temperature product for NOAA AVHRR. *Earth System Science Data, 12*, 3247-3268

Ma, L., Liu, Y., Zhang, X., Ye, Y., Yin, G., & Johnson, B.A. (2019). Deep learning in remote sensing applications: A meta-analysis and review. *Isprs Journal of Photogrammetry and Remote Sensing, 152*, 166-177

Ma, Y., Hu, Z., Xie, Z., Ma, W., Wang, B., Chen, X., Li, M., Zhong, L., Sun, F., Gu, L., Han, C., Zhang, L., Liu, X., Ding, Z., Sun, G., Wang, S., Wang, Y., & Wang, Z. (2020b). A long-term (2005–2016) dataset of hourly integrated land–atmosphere interaction observations on the Tibetan Plateau. *Earth Syst. Sci. Data, 12*, 2937-2957

Mao, K., Shi, J., Li, Z., Qin, Z., Li, M., & Xu, B. (2007). A physics-based statistical algorithm for retrieving land surface temperature from AMSR-E passive microwave data. *Science in China Series D: Earth Sciences, 50*, 1115-1120

Mao, K., Zuo, Z., Shen, X., Xu, T., Gao, C., & Liu, G. (2018). Retrieval of Land-surface Temperature from AMSR2 Data Using a Deep Dynamic Learning Neural Network. *Chinese Geographical Science, 28*, 1-11

McFarland, M.J., Miller, R.L., & Neale, C.M.U. (1990). Land surface temperature derived from the SSM/I passive microwave brightness temperatures. *IEEE Transactions on Geoscience and Remote Sensing, 28*, 839-845

Mercury, M., Green, R., Hook, S., Oaida, B., Wu, W., Gunderson, A., & Chodas, M. (2012). Global cloud cover for assessment of optical satellite observation opportunities: A HyspIRI case study. *Remote Sensing of Environment, 126*, 62-71

Metz, M., Rocchini, D., & Neteler, M. (2014). Surface Temperatures at the Continental Scale: Tracking Changes with Remote Sensing at Unprecedented Detail. *Remote Sensing, 6*, 3822-3840

Muñoz-Sabater, J., Dutra, E., Agustí-Panareda, A., Albergel, C., Arduini, G., Balsamo, G., Boussetta, S., Choulga, M., Harrigan, S., Hersbach, H., Martens, B., Miralles, D.G., Piles, M., Rodríguez-Fernández, N.J., Zsoter, E., Buontempo, C., & Thépaut, J.-N. (2021). ERA5-Land: a state-of-the-art global reanalysis dataset for land applications. *Earth System Science Data, 13*, 4349-4383

Ohmura, A., Gilgen, H., Hegner, H., Müller, G., Wild, M., Dutton, E.G., Forgan, B., Fröhlich, C., Philipona, R., Heimo, A., König-Langlo, G., McArthur, B., Pinker, R., Whitlock, C.H., & Dehne, K. (1998). Baseline Surface Radiation Network (BSRN/WCRP): New Precision Radiometry for Climate Research. *Bulletin of the American Meteorological Society, 79*, 2115-2136

Østby, T.I., Schuler, T.V., & Westermann, S. (2014). Severe cloud contamination

of MODIS Land Surface Temperatures over an Arctic ice cap, Svalbard. *Remote Sensing of Environment, 142*, 95-102

Pede, T., & Mountrakis, G. (2018). An empirical comparison of interpolation methods for MODIS 8-day land surface temperature composites across the conterminous Unites States. *Isprs Journal of Photogrammetry and Remote Sensing, 142*, 137-150

Qu, Y., Liang, S., Liu, Q., Li, X., Feng, Y., & Liu, S. (2016). Estimating Arctic sea-ice shortwave albedo from MODIS data. *Remote Sensing of Environment, 186*, 32-46

Qu, Y., Liu, Q., Liang, S., Wang, L., Liu, N., & Liu, S. (2014). Direct-Estimation Algorithm for Mapping Daily Land-Surface Broadband Albedo From MODIS Data. *IEEE Transactions on Geoscience and Remote Sensing, 52*, 907-919

Rao, Y., Liang, S., Wang, D., Yu, Y., Song, Z., Zhou, Y., Shen, M., & Xu, B. (2019). Estimating daily average surface air temperature using satellite land surface temperature and top-of-atmosphere radiation products over the Tibetan Plateau. *Remote Sensing of Environment, 234*, 111462

Shen, H., Jiang, Y., Li, T., Cheng, Q., Zeng, C., & Zhang, L. (2020). Deep learning-based air temperature mapping by fusing remote sensing, station, simulation and socioeconomic data. *Remote Sensing of Environment, 240*

Shiff, S., Helman, D., & Lensky, I.M. (2021). Worldwide continuous gap-filled MODIS land surface temperature dataset. *Sci Data, 8*, 74

Stokes, G.M., & Schwartz, S.E. (1994). The Atmospheric Radiation Measurement (ARM) Program: Programmatic Background and Design of the Cloud and Radiation Test Bed. *Bulletin of the American Meteorological Society, 75*, 1201-1221

Sun, D., & Pinker, R.T. (2005). Implementation of GOES-based land surface temperature diurnal cycle to AVHRR. *International Journal of Remote Sensing, 26*, 3975-3984

Tang, W., Zhou, J., Ma, J., Wang, Z., Ding, L., Zhang, X., & Zhang, X. (2024). TRIMS LST: a daily 1 km all-weather land surface temperature dataset for China's landmass and surrounding areas (2000–2022). *Earth System Science Data, 16*, 387-419

Tomlinson, C.J., Chapman, L., Thornes, J.E., & Baker, C. (2011). Remote sensing land surface temperature for meteorology and climatology: a review. *Meteorological Applications, 18*, 296-306

Townshend, J.R.G., Justice, C.O., Skole, D., Malingreau, J.P., Cihlar, J., Teillet, P., Sadowski, F., & Ruttenberg, S. (2007). The 1 km resolution global data set: needs of the International Geosphere Biosphere Programme†. *International Journal of Remote Sensing, 15*, 3417-3441

Wan, Z. (2014). New refinements and validation of the collection-6 MODIS land-surface temperature/emissivity product. *Remote Sensing of Environment, 140*, 36-45

Wan, Z., & Li, Z.-L. (1997). A physics-based algorithm for retrieving land-surface emissivity and temperature from EOS/MODIS data. *IEEE Transactions on Geoscience and Remote Sensing, 35*, 980-996

Wan, Z., Wang, P., & Li, X. (2010). Using MODIS Land Surface Temperature and Normalized Difference Vegetation Index products for monitoring drought in the southern Great Plains, USA. *International Journal of Remote Sensing, 25*, 61-72

Wang, N., Tang, B.-H., Li, C., & Li, Z.-L. (2010). A generalized neural network for simultaneous retrieval of atmospheric profiles and surface temperature from hyperspectral thermal infrared data, 1055-1058

Weng, Q. (2009). Thermal infrared remote sensing for urban climate and environmental studies: Methods, applications, and trends. *Isprs Journal of Photogrammetry and Remote Sensing, 64*, 335-344

Williamson, S., Hik, D., Gamon, J., Kavanaugh, J., & Flowers, G. (2014). Estimating Temperature Fields from MODIS Land Surface Temperature and Air Temperature Observations in a Sub-Arctic Alpine Environment. *Remote Sensing, 6*, 946-963

Wu, P., Su, Y., Duan, S.-b., Li, X., Yang, H., Zeng, C., Ma, X., Wu, Y., & Shen, H. (2022). A two-step deep learning framework for mapping gapless all-weather land surface temperature using thermal infrared and passive microwave data. *Remote Sensing of Environment, 277*

Wu, P., Yin, Z., Zeng, C., Duan, S., Gottsche, F.-M., Ma, X., Li, X., Yang, H., & Shen, H. (2019). Spatially Continuous and High-resolution Land Surface Temperature: A Review of Reconstruction and Spatiotemporal Fusion Techniques. *arXiv preprint arXiv:1909.09316*

Xing, Z., Li, Z.-L., Duan, S.-B., Liu, X., Zheng, X., Leng, P., Gao, M., Zhang, X., & Shang, G. (2021). Estimation of daily mean land surface temperature at global scale using pairs of daytime and nighttime MODIS instantaneous observations. *Isprs Journal of Photogrammetry and Remote Sensing, 178*, 51-67

Xu, S., & Cheng, J. (2021). A new land surface temperature fusion strategy based on cumulative distribution function matching and multiresolution Kalman filtering. *Remote Sensing of Environment, 254*, 112256

Yamamoto, S. (2005). Findings through the AsiaFlux network and a view toward the future. *Journal of Geographical Sciences, 15*, 142

Yao, R., Wang, L., Huang, X., Cao, Q., Wei, J., He, P., Wang, S., & Wang, L. (2023). Global seamless and high-resolution temperature dataset (GSHTD), 2001–2020. *Remote Sensing of Environment, 286*

Yao, Y., Liang, S., Qin, Q., Wang, K., Liu, S., & Zhao, S. (2012). Satellite detection of increases in global land surface evapotranspiration during 1984-2007. *International Journal of Digital Earth, 5*, 299-318

Yu, P., Zhao, T., Shi, J., Ran, Y., Jia, L., Ji, D., & Xue, H. (2022). Global spatiotemporally continuous MODIS land surface temperature dataset. *Sci Data, 9*, 143

Yu, W., Ma, M., Wang, X., & Tan, J. (2014). Estimating the land-surface temperature of pixels covered by clouds in MODIS products. *Journal of Applied Remote Sensing, 8*, 083525

Yuan, Q., Shen, H., Li, T., Li, Z., Li, S., Jiang, Y., Xu, H., Tan, W., Yang, Q., Wang, J., Gao, J., & Zhang, L. (2020). Deep learning in environmental remote sensing: Achievements and challenges. *Remote Sensing of Environment, 241*

Zeng, C., Long, D., Shen, H., Wu, P., Cui, Y., & Hong, Y. (2018). A two-step framework for reconstructing remotely sensed land surface temperatures contaminated by cloud. *Isprs Journal of Photogrammetry and Remote Sensing, 141*, 30-45

Zhang, D., Tang, R., Tang, B.-H., Wu, H., & Li, Z.-L. (2015). A Simple Method for Soil Moisture Determination From LST–VI Feature Space Using Nonlinear Interpolation Based on Thermal Infrared Remotely Sensed Data. *IEEE Journal of Selected Topics in Applied Earth Observations and Remote Sensing, 8*, 638-648

Zhang, H., Tang, B.-H., & Li, Z.-L. (2024). A practical two-step framework for all-sky land surface temperature estimation. *Remote Sensing of Environment, 303*

Zhang, Q., Yuan, Q., Zeng, C., Li, X., & Wei, Y. (2018). Missing Data Reconstruction in Remote Sensing Image With a Unified Spatial–Temporal–Spectral Deep Convolutional Neural Network. *IEEE Transactions on Geoscience and Remote Sensing, 56*, 4274-4288

Zhang, T., Zhou, Y., Zhu, Z., Li, X., & Asrar, G.R. (2022). A global seamless 1 km resolution daily land surface temperature dataset (2003–2020). *Earth System Science Data, 14*, 651-664

Zhang, X., Wang, D., Liu, Q., Yao, Y., Jia, K., He, T., Jiang, B., Wei, Y., Ma, H., & Zhao, X. (2019). An operational approach for generating the global land surface downward shortwave radiation product from MODIS data. *IEEE Transactions on Geoscience and Remote Sensing, 57*, 4636-4650

Zhang, X., Zhou, J., Liang, S., Chai, L., Wang, D., & Liu, J. (2020). Estimation of 1-km all-weather remotely sensed land surface temperature based on reconstructed spatial-seamless satellite passive microwave brightness temperature and thermal infrared data. *Isprs Journal of Photogrammetry and Remote Sensing, 167*, 321-344

Zhang, X., Zhou, J., Liang, S., & Wang, D. (2021). A practical reanalysis data and thermal infrared remote sensing data merging (RTM) method for reconstruction of a 1-km all-weather land surface temperature. *Remote Sensing of Environment, 260*, 112437

Zhang, Y., Liang, S., Ma, H., He, T., Wang, Q., Li, B., Xu, J., Zhang, G., Liu, X., & Xiong, C. (2023). Generation of global 1 km daily soil moisture product from 2000 to 2020 using ensemble learning. *Earth System Science Data, 15*, 2055-2079

Zhao, W., Duan, S.-B., Li, A., & Yin, G. (2019). A practical method for reducing terrain effect on land surface temperature using random forest regression. *Remote Sensing of Environment, 221*, 635-649

Zhou, D., Xiao, J., Bonafoni, S., Berger, C., Deilami, K., Zhou, Y., Frolking, S., Yao, R., Qiao, Z., & Sobrino, J. (2018). Satellite Remote Sensing of Surface Urban Heat Islands: Progress, Challenges, and Perspectives. *Remote Sensing, 11*, 48

Zhou, J., Dai, F., Zhang, X., Zhao, S., & Li, M. (2015). Developing a temporally land cover-based look-up table (TL-LUT) method for estimating land surface temperature based on AMSR-E data over the Chinese landmass. *International Journal of Applied Earth Observation and Geoinformation, 34*, 35-50

Zhou, S., Cheng, J., & Shi, J. (2022). A Physical-Based Framework for Estimating the Hourly All-Weather Land Surface Temperature by Synchronizing Geostationary Satellite Observations and Land Surface Model Simulations. *IEEE Transactions on Geoscience and Remote Sensing, 60*, 1-22